SIAM J. APPL. MATH.
Vol. 82, No. 4, pp. 1167–1193

A MULTISCALE POROMECHANICS MODEL INTEGRATING MYOCARDIAL PERFUSION AND THE EPICARDIAL CORONARY VESSELS*

NICOLÁS ALEJANDRO BARNAFI WITTWER†, SIMONE DI GREGORIO‡, LUCA DEDE'‡, PAOLO ZUNINO‡, CHRISTIAN VERGARA§, AND ALFIO QUARTERONI‡

Abstract. The importance of myocardial perfusion at the outset of cardiac disease remains largely understudied. To address this topic we present a mathematical model that considers the systemic circulation, the coronary vessels, the myocardium, and the interactions among these components. The core of the whole model is the description of the myocardium as a multicompartment poromechanics system. A novel decomposition of the poroelastic Helmholtz potential involved in the poromechanics model allows for a quasi-incompressible model that adequately describes the physical interaction among all components in the porous medium. We further provide a rigorous mathematical analysis that gives guidelines for the choice of the Helmholtz potential. To reduce the computational cost of our integrated model we propose decoupling the deformation of the tissue and systemic circulation from the porous flow in the myocardium and coronary vessels, which allows us to apply the model also in combination with precomputed cardiac displacements, obtained form other models or medical imaging data. We test the methodology through the simulation of a heartbeat in healthy conditions that replicates the systolic impediment phenomenon, which is particularly challenging to capture as it arises from the interaction of several parts of the model.

Key words. cardiac perfusion, nonlinear poromechanics, constitutive modeling

AMS subject classifications. 92C10, 68U20, 74F10

DOI. 10.1137/21M1424482

1. Introduction.

Cardiac perfusion is the blood supply of the heart muscle and it involves three components. The first one is the *cardiac tissue*, known as myocardium. The second one is the *coronary vasculature*, which carries blood from the aorta to the myocardium and then to the venous system, and it is composed of two parts: the epicardial coronary vessels, stemming from the aorta and embracing the heart, and the myocardial coronary vessels (also known as intramural coronary vessels or coronary microvasculature), carrying the blood in the tissue to the venous system. The third component is the *systemic circulation*, which carries blood to the rest of the organs. The myocardial coronary vessels present large variations of spatial scales in the range of 10–500 μm [DJBBD92, FAC16] with very different mechanical properties [AKL10a] and a complex network structure [HBRS08, LMR+10, LS12]. As a result, the pressure that drives perfusion in the coronary microvasculature is given by the combined effects of the intravessel and intramyocardial pressures [AKL10b].

*Received by the editors June 9, 2021; accepted for publication (in revised form) February 28, 2022; published electronically July 21, 2022.

https://doi.org/10.1137/21M1424482

Funding: This work was supported by the ERC. The work of the first author was partially supported by project "Modeling the heart across the 562 scales: From cardiac cells to the whole organ" PRIN 2017AXL54F 003. The work of the sixth author was supported by the ERC through ERC2016AdG, project 740132.

†Dipartimento di Matematica "F. Enriques," Università degli Studi di Milano, I-20133 Milan, Italy (nabw91@gmail.com).

‡MOX, Department of Mathematics, Politecnico di Milano, Milan, 20133, Italy (simone.digregorio@polimi.it, luca.dede@polimi.it, paolo.zunino@polimi.it, alfio.quarteroni@polimi.it).

§Laboratory of Biological Structure Mechanics (LaBS), Dipartimento di Chimica, Materiali e Ingegneria Chimica "Giulio Natta," Politecnico di Milano, Milan, Italy (christian.vergara@polimi.it).

Mathematical models have been widely used to study this problem. The complex multiscale nature of the coronary microvasculature and its interaction with the myocardium has been mainly addressed by the use of poromechanics models [HAvCR92, VSW97, Smi04, CGSMVC10, CLM+12, VYW15, PKJ+20], consisting in a continuum model [Cou04] obtained by a formal averaging of the fluid porous structure (vessels) and the solid phase (myocardium) [Whi86]. This approach does not necessitate a detailed geometric description of the vessels, which would be impossible to obtain from medical imaging in-vivo and, in any case, computationally untractable. A more accurate description can be given by multicompartment formulations, wherein a scale separation procedure allows one to consider different vessel resolutions separately (e.g., arterioles, capillaries, venules) [CLM+12, MCC+13, DGFP+20].

Epicardial coronary vessels can be modeled either in full three-dimensional (3D) resolution [KVCC+10, DGFP+20] or by means of reduced models, which can be either lumped (namely, 0D models) [WBDVN69, QRV01, FQV09, DK75, HS90, KCB85, NLL+20] or 1D [BB00, HKL+09, LNN+09, NKL18]. The main advantage of 1D models with respect to 0D ones is the ability to capture wave propagation phenomena, particularly relevant in the coronary blood dynamics [GPCP90]. Finally, systemic circulation has been often modeled as a network of 0D elements, based on RLC elements [QVV16] and Windkessel models [WLW09] considering separately the lungs (supplied by the right ventricle) from the rest of the body [BF10, HBJ+17] (supplied by the left ventricle).

The scope of our work is the creation of a new mathematical model of cardiac perfusion encompassing all of the aforementioned components and their interactions, whose layout is shown in Figure 1.1. The interaction between the intramural coronary vessels and the heart tissue is described employing a multicompartment poromechanics model, where each compartment is associated to a different length scale of blood vessels. One distinctive feature of our new model is the use of a quasi-incompressible formulation, achieved by combining the Helmholtz potential from [CLM+12] with the thermodynamically motivated energy presented in [CM14]. This combination yields a better representation of the underlying physics and, most importantly, the pressure in the coronary microvasculature results as the difference between the intravessel and intramyocardial pressures in each compartment. Our proposed poroelastic Helmholtz potential presents two further advantages: (i) it enables the straightforward use of constitutive laws already available in the literature, and (ii) it provides analytic conditions that guarantee the existence of solutions for each of the problems within the poromechanics model, namely, the mechanics and porous media equations.

Regarding blood flow in the epicardial coronaries, we consider a 0D model [QRV01, FQV09], where we generalize the standard formulation to make it better suited for arbitrary networks of vessels. Finally, we consider an additional 0D model for the circulatory system that yields a closed loop of blood flow through the body [RSA+20a, RSA+20b].

For the numerical approximation, we neglect the feedback of blood pressure on both the circulatory system and the heart mechanics. This results in a one-way coupling strategy that allows our model to be used with a prescribed myocardial displacement obtained either by an electromechanics simulation or prescribed from imaging techniques [CWH+16], with the additional advantage of greatly reducing computational costs.

This paper is structured as follows: in section 2 we present the poromechanics model for the myocardium and the novel constitutive law, in section 3 we introduce the generalized 0D coronary vessel model, in section 4 we present the coupled perfusion

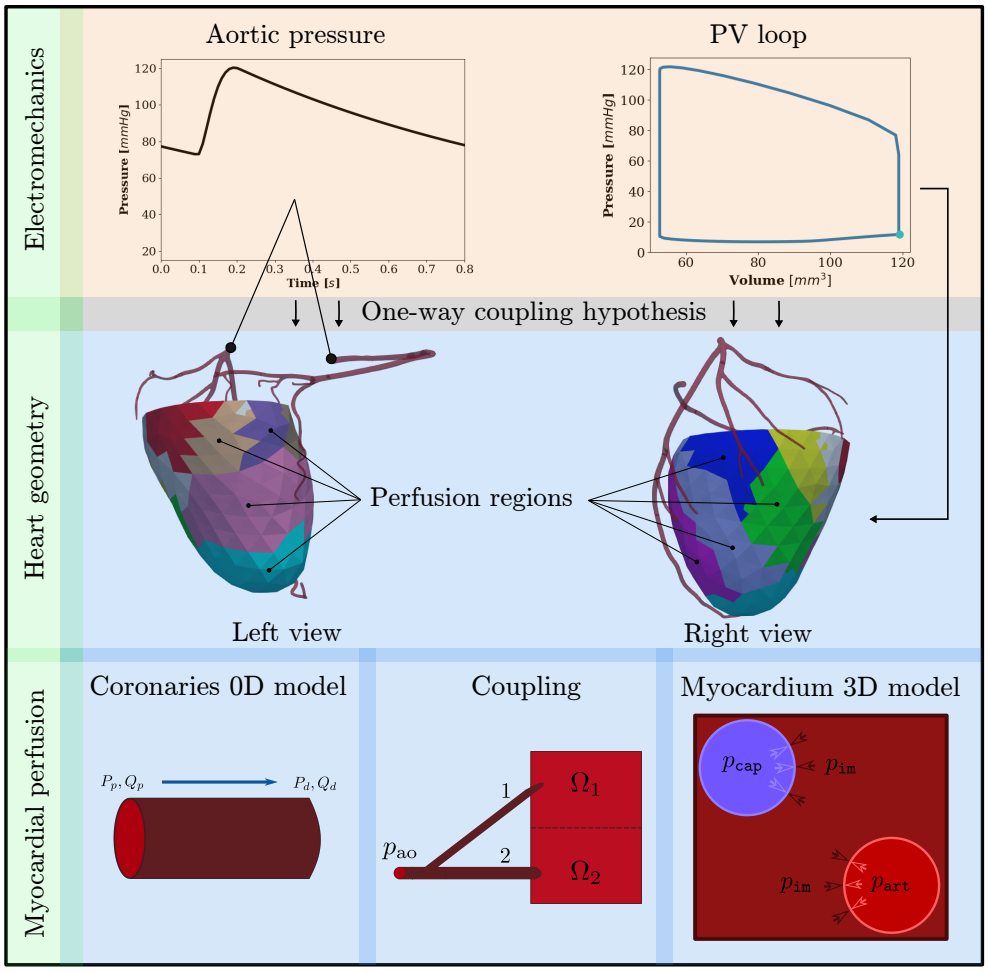

FIG. 1.1. *Description of the general layout of the integrated perfusion model and of the coupling with the heart contraction for the application to myocardial perfusion. The row "Electromechanics" shows the input used by our resulting model, meaning an electromechanics simulation coupled with a circulation model that yields the aortic pressure. The second row shows the geometry wherein the problem is solved. We neglect the feedback of perfusion on the electromechanics, which we refer to as the one-way coupling hypothesis (section* 4.1*), where aortic pressure is prescribed at the aortic root (shown in black circles connecting the aortic pressure with the vessels in "Heart geometry") and the deformation is prescribed in the myocardium (represented by the arrow connecting the PV loop and the heart geometry). Each epicardial coronary vessel perfuses an independent* perfusion region*, represented by different colors in the geometry that correspond to different vessel outlets (section* 4*). The third row shows the reduced model* 0*D used for the epicardial coronary vessels (section* 3*). "Myocardium* 3*D model" shows the multicompartment model (section* 2*), where the two compartments (arteries and capillaries) interact with the muscle through their pressures (art → artery, cap → capillary, and im → intramural), and the coupling between these components is shown in "Coupling," where a simple example depicts the flow of blood from the aortic root to two perfusion regions, where vessel* 1 *perfuses region* Ω_1 *and vessel* 2 *perfuses region* Ω_2 *(section* 4*).*

model together with the one-way coupling hypothesis, and in section 5 we perform a realistic numerical simulation to validate the proposed model.

2. Mathematical model for the myocardium and intramural coronary vessels. In this section we propose a novel constitutive model for poromechanics.

This is achieved by considering the energy contribution of the local volumes of the solid [dBCD98, CM14], the fluid phases [CLM+12], and the total volume (as in quasi-incompressible mechanics). The resulting energy yields a quasi-incompressible model that is very convenient for numerical simulations.

2.1. Poromechanics with large deformations. We review the balance laws for poromechanics by following [CM14]. For this, consider a reference domain Ω_0, deformed at time t into $\Omega(t)$ where possibly $\Omega_0 \neq \Omega(0)$. Deformation is given by a map $\boldsymbol{x}(t) : \Omega_0 \to \Omega(t)$, and we use the standard notation that $\boldsymbol{x} \coloneqq \boldsymbol{y}_s + \boldsymbol{X}$, so that $\boldsymbol{x}$ is the *current* coordinate, $\boldsymbol{X}$ is the *reference* coordinate, and $\boldsymbol{y}_s$ is the displacement. We also define the strain tensor $\boldsymbol{F} \coloneqq \nabla_{\boldsymbol{X}} \boldsymbol{y}_s$, its determinant $J \coloneqq \det \boldsymbol{F}$, and the solid velocity $\boldsymbol{v}_\mathrm{s} \coloneqq \frac{\partial \boldsymbol{y}_s}{\partial t}$.

Poromechanics is a mixture theory [Bow80, Bow82], which means that the domain of interest is composed of coexisting phases. In the context of cardiac perfusion, we consider these as a solid phase plus two fluid phases (also named *compartments*). The fluid phases correspond to the different length scales of the arteries and the capillaries. Nevertheless, the model is equally suited for an arbitrary number of fluid compartments, so we will keep the exposition general. For example, the venous system will be later modelled as a sink term, but it could be alternatively and more accurately described using an additional fluid compartment. If we consider a generic number, N_C, of fluid phases (or compartments), we can formally define a fluid volume fraction as $\phi_i \coloneqq \frac{d\Omega_{\mathrm{fluid}_i}(t)}{d\Omega(t)}$ named *porosity*, where $d\Omega_{\mathrm{fluid}_i}$ represents the differential volume of compartment i, and a solid volume fraction $\phi_s \coloneqq 1 - \sum_{i=1}^{N_C} \phi_i$. These quantites relate the phase measure to the Lebesgue measure through $d\Omega_{\mathrm{fluid}_i}(t) = \phi_i d\Omega(t)$. Their reference counterpart, i.e., the Lagrangian porosities given by $\varphi_i \coloneqq J\phi_i$, are the primary variables regarding mass conservation. The initial and solid Lagrangian porosities are then given by $\varphi_{i,0} = J_0\phi_{i,0}$ and $\varphi_s = J - \sum_{i=1}^{N_C} \varphi_i$ respectively, so we denote with $\varphi_{s,0} = J_0 - \sum_{i=1}^{N_C} \varphi_{i,0}$ the initial solid Lagrangian porosity.

Mass conservation. We consider a compartment $i \in \{1, ..., N_C\}$, a distributed mass source term θ_i associated to the fluid phase, and define the fluid, solid, and total densities as $\rho_{f,i}, \rho_s$, and $\rho \coloneqq \phi_s\rho_s + \sum_{i=1}^{N_C} \phi_i\rho_{f,i}$, respectively.

We additionally define the reference density of added mass m_i in Ω_0 as the difference between the fluid content in current and initial configurations, $m_i \coloneqq \rho_{f,i}(\varphi_i - \varphi_{i,0})$, with which we obtain mass conservation in each compartment i as

$$\frac{dm_i}{dt} + \mathrm{div}_{\boldsymbol{X}}(\boldsymbol{W}_i) = \Theta_i - J\sum_{j=1}^{N_C} \beta_{ij}(p_i - p_j) \quad \text{in} \quad \Omega_0, \tag{2.1}$$

where $\Theta_i \coloneqq J\theta_i$ is the reference source term for a current distributed mass source θ_i, $\boldsymbol{W}_i \coloneqq \rho_{f,i}\phi_i\boldsymbol{V}_{r,i}$ is the reference flow vector, $\boldsymbol{V}_{r,i} \coloneqq J\boldsymbol{F}^{-1}(\boldsymbol{v}_{f,i} - \boldsymbol{v}_\mathrm{s})$ is the reference relative velocity, β_{ij} is an intercompartment interaction coefficient, and pressure is obtained through constitutive modeling from a Helmholtz potential Ψ as $p_i = \frac{\partial \Psi}{\partial \varphi_i}$. We note that the added mass density m_i and Lagrangian porosity φ_i are related by an affine transformation, so both are valid candidates for being primary variables. Still, the Lagrangian porosity is preferable as it is dimensionless and, as seen from the definition of the pressure, it is also the natural thermodynamic quantity of this model.

The flow vector can be obtained from the pressure gradient through a Darcy law by means of a permeability tensor $\tilde{\boldsymbol{k}}_{f,i}$, given by

$$\boldsymbol{W}_i = -\rho_{f,i}J\boldsymbol{F}^{-1}\tilde{\boldsymbol{k}}_{f,i}\boldsymbol{F}^{-T}\nabla_{\boldsymbol{X}} p_i = -\rho_{f,i}\boldsymbol{K}_{f,i}\nabla_{\boldsymbol{X}} p_i, \tag{2.2}$$

where we defined the Lagrangian permeability tensor $\boldsymbol{K}_{f,i} \coloneqq J\boldsymbol{F}^{-1}\tilde{\boldsymbol{k}}_{f,i}\boldsymbol{F}^{-T}$. We consider a no-slip boundary condition, given by

$$\boldsymbol{W}_i \cdot \boldsymbol{n} = -\rho_{f,i}\boldsymbol{K}_{f,i}\nabla_{\boldsymbol{X}} p_i = 0 \quad \text{on} \quad \partial\Omega_0.$$

Conservation of momentum. We consider the standard conservation of momentum in quasi-static form, given by

$$-\operatorname{div}_{\boldsymbol{X}} \boldsymbol{P}_{\text{tot}} = \boldsymbol{0} \qquad \text{in} \quad \Omega_0, \tag{2.3}$$

where $\boldsymbol{P}_{\text{tot}}$ is the total Piola stress tensor. In cardiac modeling, the stress tensor considers both passive and active mechanics, so we adopt an active stress approach [QLRRB17, AANQ11] which yields $\boldsymbol{P}_{\text{tot}} = \boldsymbol{P} + \boldsymbol{P}_a$, where $\boldsymbol{P}_a$ models the active mechanics and $\boldsymbol{P}$, obtained from constitutive modeling as $\boldsymbol{P} = \frac{\partial \Psi}{\partial \boldsymbol{F}}$, models the passive mechanics. For the boundary, we consider a Robin condition which accounts for the friction with the pericardium and the effect of the atria at the base [ULM02]:

$$\boldsymbol{P}_{\text{tot}}\boldsymbol{n} + k_\perp \boldsymbol{f}_0 \otimes \boldsymbol{f}_0 \boldsymbol{y}_s + k_\parallel (\boldsymbol{I} - \boldsymbol{f}_0 \otimes \boldsymbol{f}_0)\boldsymbol{y}_s = 0 \qquad \text{on} \quad \partial\Omega_0, \tag{2.4}$$

where $k_\perp = 2\,10^5$ Pa and $k_\parallel = 0.1\,k_\perp$ [PHW+19]. We denote it by $\boldsymbol{P}_{\text{tot}}\boldsymbol{n} = \boldsymbol{g}(\boldsymbol{y}_s)$ on Ω_0. The active stress term is given by a fiber-oriented force:

$$\boldsymbol{P}_a(\boldsymbol{F}, t) = \gamma(t)\frac{(\boldsymbol{F}\boldsymbol{f}_0) \otimes \boldsymbol{f}_0}{|\boldsymbol{F}\boldsymbol{f}_0|},$$

where $|\boldsymbol{x}| \coloneqq \sqrt{\boldsymbol{x} \cdot \boldsymbol{x}}$, $\boldsymbol{f}_0$ represents a fiber orientation and γ, possibly also space dependent, represents the activation of the cardiomyocites (heart muscle cells), driven by the heart's electrophysiology. Further details on these topics can be found in [BBPT12] and [FPS14], respectively. We note also that in (2.3) we have considered a quasi-static formulation, which neglects the inertia term. In electromechanics, it is well known that inertia is negligible [CCHK17], but a similar systematic analysis has not been applied to cardiac perfusion yet.

The multicompartment model. In what follows, we consider all quantities in reference configuration and thus drop the subindex from differential operators as $\nabla = \nabla_{\boldsymbol{X}}, \operatorname{div} = \operatorname{div}_{\boldsymbol{X}}$. Putting everything together, the multicompartment poromechanics model is given as follows: Find a displacement $\boldsymbol{y}_s$ and Lagrangian porosities $\boldsymbol{\varphi} = (\varphi_1, ..., \varphi_{N_C})$ such that for each $t > 0$ it holds that

$$-\operatorname{div}(\boldsymbol{P}(\boldsymbol{F}, \boldsymbol{\varphi}) + \boldsymbol{P}_a(\boldsymbol{F})) = \boldsymbol{0} \qquad \text{in} \quad \Omega_0, \tag{2.5a}$$

$$\begin{aligned} &\frac{d\varphi_i}{dt} - \operatorname{div}\left(\boldsymbol{K}_i(\boldsymbol{F})\nabla_{\boldsymbol{X}} p_i(\boldsymbol{F}, \boldsymbol{\varphi})\right) \\ &+ J\sum_{j=1}^{N_C} \beta_{ij}(p_i(\boldsymbol{F}, \boldsymbol{\varphi}) - p_j(\boldsymbol{F}, \boldsymbol{\varphi})) = J\theta_i \qquad \text{in} \quad \Omega_0, \quad \forall i \in \{1, ..., N_C\}, \end{aligned} \tag{2.5b}$$

$$(\boldsymbol{P} + \boldsymbol{P}_a)\boldsymbol{n} = \boldsymbol{g}(\boldsymbol{y}_s) \qquad \text{on} \quad \partial\Omega_0, \tag{2.5c}$$

$$\rho_{f,i}\boldsymbol{K}_{f,i}(\boldsymbol{F})\nabla_{\boldsymbol{X}} p_i \cdot \boldsymbol{n} = 0 \qquad \text{on} \quad \partial\Omega_0 \quad \forall i \in \{1, ..., N_C\}, \tag{2.5d}$$

$$\boldsymbol{\varphi}(0) = \boldsymbol{\varphi}_0 \qquad \text{in} \quad \Omega_0. \tag{2.5e}$$

2.2. Constitutive modeling. In nonlinear poroelasticity with incompressible fluids, the Piola stress tensor $\boldsymbol{P}$ and the compartment pressures p_i for $i \in \{1, ..., N_C\}$ are obtained from a Helmholtz potential Ψ [Cou04, CLM+12]:

$$\boldsymbol{P}(\boldsymbol{F}, \boldsymbol{\varphi}) = \frac{\partial \Psi}{\partial \boldsymbol{F}}(\boldsymbol{F}, \boldsymbol{\varphi}), \quad p_i(\boldsymbol{F}, \boldsymbol{\varphi}) = \frac{\partial \Psi}{\partial \varphi_i}(\boldsymbol{F}, \boldsymbol{\varphi}). \tag{2.6}$$

The main approaches for constitutive modeling in cardiac poromechanics are based on additive splittings of the Helmholtz potential Ψ. In what follows, we present a brief review of such models to motivate the proposal of a new one which yields fully quasi-incompressible poromechanics, i.e., without the imposition of incompressibility constraints on any of the phases involved.

Additive splitting with fluid porosity [CLM+12]. This approach decomposes the energy into skeleton and fluid parts. This is achieved by considering one potential for the solid phase ψ_{skel} and one for each fluid compartment ψ_i as

$$\tilde{\Psi}_A(\boldsymbol{F}, \boldsymbol{\varphi}) = \psi_{\text{skel}}(\boldsymbol{F}) + \sum_{i=1}^{N_C} \psi_i(\varphi_i), \tag{2.7}$$

which does not account for the interaction between the porous media and the mechanics. This limitation is circumvented in [CLM+12] by the use of a Lagrange multiplier λ with respect to the incompressibility of the solid phase $J = J_0 + \sum_{i=1}^{N_C} m_i/\rho_f$, so the modified energy becomes

$$\Psi_A(\boldsymbol{F}, \boldsymbol{\varphi}) = \psi_{\text{skel}}(\boldsymbol{F}) + \sum_{i=1}^{N_C} \psi_i(\varphi_i) - \lambda \left(J - J_0 - \sum_{i=1}^{N_C} m_i/\rho_f \right), \tag{2.8}$$

which yields

$$\boldsymbol{P}(\boldsymbol{F}, \boldsymbol{\varphi}) = \frac{\partial \psi_{\text{skel}}}{\partial \boldsymbol{F}}(\boldsymbol{F}) - \lambda J \boldsymbol{F}^{-T}, \quad p_i(\boldsymbol{F}, \boldsymbol{\varphi}) = \frac{\partial \psi_i}{\partial \varphi_i}(\varphi_i) + \lambda.$$

This indeed allows for the recovery of the interaction between physics, but adds two difficulties. On one side, a constrained problem results in a saddle point problem that is in general more difficult to approximate numerically. On the other side, there is a lack of control on λ from the modeling point of view which makes it difficult to model the pressure response due to deformation. In addition, the functions ψ_i are such that $\lim_{\varphi_i \to 0} \psi_i(\varphi_i) = \infty$ and so $\phi_i > 0$ for all $i \in \{1, ..., N_C\}$, but do not guarantee that $\sum_{j=1}^{N_C} \phi_j < 1$.

Additive splitting with solid porosity [CM14]. This approach, based on [dBCD98], considers a decomposition of the energy into a skeleton part and a solid porosity part. It reads

$$\Psi_B(\boldsymbol{F}, \varphi) = \psi_{\text{skel}}(\boldsymbol{F}) + \psi_s(\varphi_s), \tag{2.9}$$

and it depends only on the solid porosity. This formulation captures the feedback of the skeleton on the fluid and vice-versa:

$$\boldsymbol{P}(\boldsymbol{F}, \boldsymbol{\varphi}) = \frac{\partial \psi_{\text{skel}}}{\partial \boldsymbol{F}}(\boldsymbol{F}) + \frac{\partial \psi_s}{\partial \varphi_s}(\varphi_s) J \boldsymbol{F}^{-T}, \quad p_i(\boldsymbol{F}, \boldsymbol{\varphi}) = -\frac{\partial \psi_s}{\partial \varphi_s}(\varphi_s), \tag{2.10}$$

but it presents two drawbacks. The first one is that the pressure expression is the same for each compartment i, and the second one is that the resulting problem is degenerate parabolic, with no control over the single compartment. To see the last point, we consider only mass conservation (2.18) on each compartment, with $\boldsymbol{K} = \boldsymbol{I}$, $\rho_f = 1$, no compartment interaction ($\beta_{ik} = 0$), and no source term ($\Theta_i = 0$). Thus we can recast the mass conservation in the ith compartment as

$$\frac{\partial \varphi_i}{\partial t} + \operatorname{div}\left(\frac{\partial p}{\partial \varphi_s} \nabla \varphi_s \right) = 0,$$

where we used $\nabla p = \frac{\partial p}{\partial \varphi_s}\nabla\varphi_s$. If we assume that the potential ψ_s is strictly convex with $\frac{\partial^2 \psi_s}{\partial \varphi_s^2} \geq \psi_0 > 0$, then by testing each equation by a test function q_i in $H_0^1(\Omega_0)$, denoting the L^2 inner product with $(\cdot,\cdot)$, and focusing only on the differential operator, we see that the problem is degenerate parabolic, as we obtain control only on the sum of the (fluid) porosities:

$$\left(\frac{\partial^2 \psi_s}{\partial \varphi_s^2}\left(\sum_{i=1}^{N_c}\nabla\varphi_i\right), \left(\sum_{i=1}^{N_c}\nabla\varphi_i\right)\right) \geq \psi_0 \left\|\sum_{i=1}^{N_c}\nabla\varphi_i\right\|^2_{L^2(\Omega_0)}$$

for all $\varphi_i \in H^1(\Omega_0)$. In contrast to the previous model, this one yields $\phi_s(\varphi_s) \to \infty$ as $\phi_s \to 1$ and thus guarantees $\sum_{j=1}\phi_j < 1$, but it fails to enforce $\phi_i > 0$ for all $i \in \{1, ..., N_C\}$.

In what follows we propose a new strategy for devising a poroelastic potential Ψ that overcomes the disadvantages of the previous ones.

New additive splitting with fluid and solid porosities. We consider a new decomposition that combines the previous approaches:

$$\Psi(\boldsymbol{F}, \boldsymbol{\varphi}) = \overbrace{\psi_{\text{skel}}(\boldsymbol{F}) + \underbrace{\psi_s(\varphi_s) + \sum_{i=1}^{N_C}\psi_i(\varphi_i)}_{\text{porous media}}}^{\text{mechanics}}.$$

This gives the relations

$$\boldsymbol{P}(\boldsymbol{F}, \boldsymbol{\varphi}) = \frac{\partial \psi_{\text{skel}}}{\partial \boldsymbol{F}}(\boldsymbol{F}) + \frac{\partial \psi_s(\varphi_s)}{\partial \varphi_s} J\boldsymbol{F}^{-T}, \quad p_i(\boldsymbol{F}, \boldsymbol{\varphi}) = \frac{\partial \psi_i}{\partial \varphi_i}(\varphi_i) - \frac{\partial \psi_s}{\partial \varphi_s}(\varphi_s), \tag{2.11}$$

from which we highlight the following aspects:

1. The porous part $\psi_s + \sum_i \psi_i$ acts as a double barrier potential constraining the porosity such that $0 < \phi_i$ for all $i \in \{1, ..., N_C\}$ and $\sum_{j=1}^{N_C}\phi_j < 1$.
2. The pressure-like term $\frac{\partial \psi_s(\varphi_s)}{\partial \varphi_s} J\boldsymbol{F}^{-T}$ appearing in the Piola stress tensor is driven by the pressure in the solid portion of the tissue φ_s only.
3. The pressure acting on the blood is the difference between the one in the compartment (luminar) and the one in the tissue (intramyocardial). It is known as transmural pressure and is correctly captured from the proposed potential:

$$p_i(\boldsymbol{F}, \boldsymbol{\varphi}) = \underbrace{\frac{\partial \psi_i}{\partial \varphi_i}(\varphi_i)}_{\text{luminar pressure}} - \underbrace{\frac{\partial \psi_s}{\partial \varphi_s}(\varphi_s)}_{\text{intramyocardial pressure}}.$$

This shows why we have called such decomposition *fully* incompressible: there can coexist two penalization terms, $\psi_s(\varphi_s)$ imposing $\varphi_s \approx \varphi_{s,0}$ and possibly a term $\psi(J)$ included in ψ_{skel} enforcing $J \approx J_0$. This effect is indeed desirable, as it models both the solid phase incompressibility and the stress contribution which produces work on deformations associated with changes of volumes [CM14].

Remark 2.1. The potential ψ_s yields a similar interaction to that of the Lagrange multiplier λ used in the model of additive splitting with fluid porosity. In fact, the multiplier imposes the constraint $\varphi_s = \varphi_{s,0}$, which is the quantity penalized by the potential ψ_s.

2.3. Constitutive model used for cardiac perfusion. We present expressions for $\psi_{\text{skel}}, \psi_s$, and $\psi_i, i = 1, \dots, N_C$, defined in section 2.2, which are adequate for cardiac poromechanics. We highlight that the proposed constitutive model allows for all energy terms to be obtained from existing literature.

Skeleton energy. We consider a Guccione constitutive law [GMW91], given by

$$\psi_{\text{skel}}(\boldsymbol{F}) = C_{\text{el}} \exp\{Q(\boldsymbol{F}) - 1\} + \frac{\kappa}{2}(J-1)\log J, \tag{2.12}$$

$$Q = b_f E_{ff}^2 + b_s E_{ss}^2 + b_n E_{nn}^2 + 2(b_{fs} E_{fs}^2 + b_{fn} E_{fn}^2 + b_{sn} E_{sn}^2), \tag{2.13}$$

$$\boldsymbol{E} = \frac{1}{2}(\boldsymbol{F}^T \boldsymbol{F} - \boldsymbol{I}), \boldsymbol{F} = \nabla \boldsymbol{y}_s + \boldsymbol{I}, E_{uv} = (\boldsymbol{E}\boldsymbol{v}) \cdot \boldsymbol{u}, \tag{2.14}$$

where $\boldsymbol{f}, \boldsymbol{s}$, and $\boldsymbol{n}$, referred to in the subindexes of $\boldsymbol{E}$ in (2.13), are a pointwise set of independent vectors directed toward the heart fibers, sheets, and normal directions [BBPT12].

Solid phase energy. The term ψ_s represents a penalization on the solid Lagrangian porosity φ_s. Its role is similar to that of the quasi-incompressibility term included in ψ_{skel}, and for it we adapt the expression used in [BCM17]:

$$\psi_s = \kappa_s \left(\varphi_s - \varphi_{s,0} - \log\left(\frac{\varphi_s}{\varphi_{s,0}} \right) \right).$$

Fluid compartments energy. Functional relations between pressure and intramural vessel volume have been proposed in [BADS88] and were obtained by fitting (real) data. In [BADS88], such laws were proposed for a three-compartment 0D model of the heart composed of (myocardial coronary) arteries, capillaries, and veins, which makes it a perfect candidate for our multicompartment framework. We consider only the arteries and capillaries and thus $N_C = 2$, so for clarity in what follows, we will replace the numeral subscripts "1" and "2" with "art" and "cap" whenever we describe the compartments separately. Such laws, although devised to represent the coronary pressure, present no dependence on the myocardium (i.e., φ_s), so we consider them instead as the fluid compartment energies. This results in the following relationship for each compartment $i \in \{1, 2\}$:

$$\psi_i(\varphi_i) = c_{i,1} \exp(c_{i,3}\varphi_i) + c_{i,2} \log(c_{i,3}\varphi_i). \tag{2.15}$$

Prestress and myocardial pressure. The reference configuration given by the null displacement $\Omega_0 \coloneqq \Omega(\boldsymbol{0})$ is most probably not in equilibrium when considering the inner stresses and the blood pressure in the heart chambers. This has motivated the computation of an initial configuration $\Omega(\boldsymbol{y}_{s0})$ known as the *prestress* configuration, which is in mechanic equilibrium [HB11, GDQ19, DGQ20] and is usually associated to the end of diastole. We propose extending the same principle to the compartment pressure p_i, meaning that the prestress configuration is in pressure equilibrium in each compartment. This can be achieved by rescaling the pressure laws with respect to reference pressures $p_{\text{ref,i}}$. For this, we denote the prestress displacement and initial Lagrangian porosities as $\boldsymbol{y}_{s0}$ and $\boldsymbol{\varphi}_0$, respectively, and impose that $p_i(\boldsymbol{F}_0, \boldsymbol{\varphi}_0) = p_{\text{ref,i}}$, which results in a rescaled pressure $\tilde{p}_i$:

$$\tilde{p}_i(\boldsymbol{F}, \boldsymbol{\varphi}) = p_i(\boldsymbol{F}, \boldsymbol{\varphi}) - p_i(\boldsymbol{F}_0, \boldsymbol{\varphi}_0) + p_{\text{ref,i}}.$$

Note that this is an intracompartment balance, as flow between compartments is still possible if there is a pressure difference between them.

2.4. Mathematical properties of the poromechanics model. The mathematical analysis of problem (2.5) is still open. System (2.5) consists in the coupling of two well-known problems, the nonlinear quasi-static mechanics (2.5a) and the porous media equation (2.5b), which pose well established regularity requirements on the form of the Helmholtz potential Ψ. In this section, in view of the well posedness analysis, we (i) ignore the Robin condition (2.4) and consider a homogeneous Dirichlet boundary condition on $\partial\Omega$, (ii) disregard the active stress, i.e., $P_a = 0$, and (iii) consider a mono-compartment system ($N_C = 1$) with $\boldsymbol{K}_f = \boldsymbol{I}/(J\rho_f), \rho_f = 1$, and $\Theta_1 = 0$. We study both subproblems, mechanics and porous media, separately.

The mechanics subproblem. We first observe that problem (2.5a) can be reformulated as a minimization problem: given a function φ, find a minimizer $\boldsymbol{y}_s$ of

$$\min_{\boldsymbol{y}_s \in \mathbf{W}} \int_\Omega \Psi_S(\boldsymbol{F}, \varphi)\, dX, \tag{2.16}$$

where $\mathbf{W} = \{\boldsymbol{y}_s{}^* \in \boldsymbol{W}^{1,1}(\Omega) : \boldsymbol{P}(\boldsymbol{F}(\boldsymbol{y}_s{}^*))\boldsymbol{n} = \boldsymbol{g}(\boldsymbol{y}_s{}^*) \text{ on } \partial\Omega_0, \Psi_S(\boldsymbol{y}_s{}^*) < \infty\}$. The existence of minimizers of problem (2.16) can be established in virtue of the following well-known result [MQY94], which we adapted to consider the dependence on φ.

THEOREM 2.2. *For every Lagrangian porosity φ assume the following hypotheses hold:*

$(HS)_1$ *Ψ_S is polyconvex, so there exists a convex function G_φ defined in $\mathbb{R}^{d\times d} \times \mathbb{R}^{d\times d} \times \mathbb{R}$ such that*

$$\Psi_S(\boldsymbol{F}, \varphi) = G_\varphi(\boldsymbol{F}, \operatorname{cof} \boldsymbol{F}, \det \boldsymbol{F}), \tag{2.17}$$

where $\operatorname{cof} \boldsymbol{F} = \det(\boldsymbol{F})\boldsymbol{F}^{-T}$.

$(HS)_2$ *Ψ_S is a Carathéodory function, i.e., $\boldsymbol{F} \to \Psi_S(\boldsymbol{X}, \boldsymbol{F}, \varphi)$ is continuous and $\boldsymbol{X} \to \Psi_S(\boldsymbol{X}, \boldsymbol{F}, \varphi)$ is measurable with $\Psi_S = \infty$ if and only if $J \le 0$.*

$(HS)_3$ *Ψ_S is coercive, meaning that there exist constants $a > 0, p \ge 2, q \ge 3/2$ such that*

$$\Psi_S(\boldsymbol{X}, \boldsymbol{F}, \varphi) \ge a(|\boldsymbol{F}|^p + |\operatorname{cof} \boldsymbol{F}|^q).$$

Then, if $\mathbf{W} \neq \emptyset$, Ψ_S attains its minimum in $\mathbf{W}$.

The law proposed in (2.11) yields the following potential for the mechanics:

$$\Psi_S(\boldsymbol{F}, \varphi) \coloneqq \psi_{\text{skel}}(\boldsymbol{F}) + \psi_s(\varphi_s).$$

We note that if ψ_{skel} is polyconvex and ψ_s is convex, then Ψ_S is polyconvex as well, which grants the existence of minimizers for problem (2.16). We stress that there are no growth conditions for the potential ψ_s with respect to J.

Porous media subproblem. Under the stated hypotheses, problem (2.5b) becomes the following: given $\boldsymbol{F}$, find φ such that

$$\frac{\partial \varphi}{\partial t} - \operatorname{div}(\nabla p(\boldsymbol{F}, \varphi)) = 0 \quad \text{in} \quad \Omega_0, \tag{2.18}$$

where $p = \frac{\partial \Psi_P}{\partial \varphi}$ is a given function. The existence of solutions is a consequence of the following result [Váz07], which we have adapted to include the dependence on $\boldsymbol{F}$.

THEOREM 2.3. *For each $\boldsymbol{F}$, assume the following hypotheses:*

$(HP)_1$ *The pressure function $\varphi \mapsto p(\boldsymbol{F}, \varphi)$ is continuous and strictly increasing in φ with $p(0) = 0$.*

$(HP)_2$ *The pressure function* $\varphi \mapsto p(\boldsymbol{F}, \varphi)$ *is smooth with* $\frac{\partial p}{\partial \varphi} > 0$ *for* $\varphi > 0$.
If the initial data $\varphi(0)$ *is such that* $\varphi(0) \geq 0, \varphi(0) \in L^1(\Omega_0)$, *and* $\Psi_P(\boldsymbol{F}, \varphi(0)) \in L^1(\Omega_0)$ *for all* $\boldsymbol{F}$, *then there exists a unique weak solution of problem* (2.18).

The model proposed in (2.11) yields the porous potential

$$\Psi_P(\boldsymbol{F}, \varphi) \coloneqq \psi_s(\varphi_s) + \psi(\varphi),$$

which is convex in the variable φ if both ψ_s and ψ are convex. In such a case, an additional smoothness assumption guarantees that hypotheses $(HP)_1$ and $(HP)_2$ are satisfied, where we observe that the normalization condition in $(HP)_1$ holds due to the consideration of the prestress configuration discussed in section 2.3.

The poromechanics problem. Putting the previous theories together, it follows that the existence of solutions to problems (2.18) and (2.16) (separately) is guaranteed under the following unified hypotheses:

- $(H)_1$ ψ_{skel} is a polyconvex and coercive Carathéodory function.
- $(H)_2$ ψ_s is a smooth and convex Carathéodory function such that $\psi_s = \infty$ if and only if $J \leq 0$.
- $(H)_3$ ψ is a smooth convex function.
- $(H)_4$ Ψ_P satisfies the normalization condition $\frac{\partial \Psi_P}{\partial \varphi}(0) = 0$.

Indeed, $(H)_1$ and $(H)_2$ guarantee $(HS)_1, (HS)_2$, and $(HS)_3$; $(H)_2$, $(H)_3$, and $(H)_4$ instead guarantee $(HP)_1$ and $(HP)_2$. Note also that the convexity of φ_s grants both the convexity of $J \mapsto \psi_s(\varphi_s)$ and $\varphi \mapsto \psi(\varphi_s)$.

This result has two fundamental consequences. From the modeling point of view, it provides useful guidelines for devising the poromechanics potentials proposed in section 2.2. Most notably, our model is capable of combining the properties of both physics, meaning the polyconvexity from the mechanics and the convexity from the porous media. In addition, from the numerical point of view, we can consider block-partitioned iterative schemes for the solution of the coupled problem. For instance, this can be achieved by considering a quasi-Newton method where the Jacobian matrix is approximated by its diagonal (or triangular) blocks. In such case, each of the diagonal blocks will be invertible. Alternatively, one could consider a one-way coupling that solves first the mechanics and then the porous media, which is indeed what we do as we know a priori that existence is guaranteed for both problems. More details are in section 4.1.

3. Mathematical modeling of the epicardial coronary vessels. In this section we present a mathematical model for the epicardial coronary vessels by means of the classic lumped 0D model [QVV16, QDMV19], which is obtained by means of a volumetric averaging of the Navier–Stokes equations in a compliant domain. This approach considers each vessel portion as an independent segment, with pressure and flow as averaged quantities in each segment. The coupling of the segments is done by means of transmission conditions given by mass conservation and pressure continuity. More complex 0D coronary circulation models have been proposed, such as the intramyocardial pump model [SBL81]. However, here we are interested only in a 0D epicardial coronary model, since the intramural vessels are considered through a poroelastic model. To make the model more flexible with respect to the boundary and coupling conditions, we consider the problem variables (volumetric flow and pressure) as being a convex combination of the corresponding proximal and distal quantities.

3.1. Single vessel model. We characterize a single vessel segment with the following parameters: length ℓ, area A, wall thickness H, fluid density ρ_f, Young

modulus of the vessel wall E, Poisson ratio of vessel wall ν, and fluid viscosity μ_f. The resulting mass and momentum conservation equations for each $t > 0$ are given by [QVV16]

$$L\frac{dQ}{dt} + RQ + P_d - P_p = 0, \tag{3.1a}$$

$$C\frac{dP}{dt} + Q_d - Q_p = 0, \tag{3.1b}$$

$$Q(0) = Q_0, \tag{3.1c}$$

$$P(0) = P_0, \tag{3.1d}$$

where $R = \frac{K_r \ell}{A^2}$, $L = \frac{\rho_f \ell}{A}$, $C = \frac{A^{3/2}\ell}{\eta}$ and $K_r = 8\pi\mu_f, \eta = \frac{\sqrt{\pi}HE}{1-\nu^2}$, with the names R, L, C coming from an analogy with these equations to an RLC circuit. The variables are the volumetric flow rate Q and the mean pressure P, whereas quantities with the subindices d, p stand for distal and proximal variables; see Figure 1.1 in the Coronaries 0D model frame.

In using this model, it is common practice to approximate the averaged quantities with one of the extremes, for instance, $Q \approx Q_d$ and $P \approx P_p$. This procedure results in four different types of well-known segment models, each one corresponding to a different combination of boundary conditions[1] on Q (Dirichlet) and P (Neumann). In addition, other types of boundary conditions can be of interest, such as the Robin type, for which no analogy with an electrical circuit is possible. We propose to consider in each vessel segment two constants α and β in $[0, 1]$ allowing us to interpolate between the distal and proximal quantities and resulting in a generalization of all possible scenarios of boundary conditions:

$$Q = \alpha Q_d + (1-\alpha)Q_p \quad \text{and} \quad P = \beta P_d + (1-\beta)P_p.$$

This yields the following modified form of (3.1a) and (3.1b):

$$\begin{aligned} L\frac{d\left(\alpha Q_d + (1-\alpha)Q_p\right)}{dt} + R(\alpha Q_d + (1-\alpha)Q_p) + P_d - P_p = 0, \\ C\frac{d\left(\beta P_d + (1-\beta)P_p\right)}{dt} + Q_d - Q_p = 0. \end{aligned} \tag{3.2}$$

Remark 3.1. If $L = C = 0$, we obtain the well-known Poiseuille flow, which loses dependence on α and β.

We recall that the 0D model is obtained from the Navier–Stokes equations on a compliant 3D cylinder under suitable assumptions. The resulting problem has four unknowns (Q_d, Q_p, P_d, P_p), and so (3.2) must be closed with two additional constraints. These are provided by the inlet and outlet boundary conditions of the 3D Navier–Stokes problem in the cylinder in reduced form. In particular, note that Dirichlet conditions are reduced to fixing Q_d or Q_p (outlet or inlet), whereas Neumann boundary conditions pertain to P_d or P_p (outlet or inlet). The proposed model can handle all such scenarios, so in what follows, we consider the model abstractly, with these two extra constraints chosen.

[1]The expression "boundary condition" is widely used in this context. It is of course not a precise notion, as a 0D model has no boundary, but it describes the fact that the conditions required to close the model are given by inlet (proximal) and outlet (distal) quantities, as given for the starting 3D model.

By denoting the unknown as $\boldsymbol{Z} = (Q_d, Q_p, P_d, P_p)^T$, this problem can be rewritten as a set of differential algebraic equations:

$$\begin{aligned} \boldsymbol{E}\dot{\boldsymbol{Z}}(t) + \boldsymbol{H}\boldsymbol{Z}(t) &= \boldsymbol{b}(t), \\ P(0) &= P_0, \\ Q(0) &= Q_0, \end{aligned} \tag{3.3}$$

where

$$\boldsymbol{E} \coloneqq \begin{bmatrix} \alpha L & (1-\alpha)L & 0 & 0 \\ 0 & 0 & \beta C & (1-\beta)C \\ 0 & 0 & 0 & 0 \\ 0 & 0 & 0 & 0 \end{bmatrix}, \boldsymbol{H} \coloneqq \begin{bmatrix} \alpha R & (1-\alpha)R & 1 & -1 \\ 1 & -1 & 0 & 0 \\ \gamma_{1qd} & \gamma_{1qp} & \gamma_{1pd} & \gamma_{1pp} \\ \gamma_{2qd} & \gamma_{2qp} & \gamma_{2pd} & \gamma_{2pp} \end{bmatrix}, \boldsymbol{b}(t) = \begin{bmatrix} 0 \\ 0 \\ b_3(t) \\ b_4(t) \end{bmatrix}.$$

Constants b_3, b_4 stand for the additional constraints representing the boundary conditions. Regarding the values of γ_{ijk}, we idenify the four classic types of boundary conditions for the starting 3D model according to the distal and proximal conditions:

(DD) Dicihlet and Dirichlet, $\gamma_i = \begin{cases} 1, & i \in \{1qd, 2qp\}, \\ 0 & \text{elsewhere.} \end{cases}$	**(ND)** Neumann and Dirichlet, $\gamma_i = \begin{cases} 1, & i \in \{1qd, 2pp\}, \\ 0 & \text{elsewhere.} \end{cases}$
(DN) Dirichlet and Neumann, $\gamma_i = \begin{cases} 1 & i \in \{1pd, 2qp\}, \\ 0 & \text{elsewhere.} \end{cases}$	**(NN)** Neumann and Neumann, $\gamma_i = \begin{cases} 1 & i \in \{1pd, 2pp\}, \\ 0 & \text{elsewhere.} \end{cases}$

In all cases, the existence of a solution of (3.3) is guaranteed:

Proof. We only show the proof for the (DD) case; the others are proved analogously. We use [Cam80, Theorem 3.1.1], so it suffices to show that there exists $s > 0$ such that $(s\boldsymbol{E} + \boldsymbol{H})$ is invertible. Setting $s > 0$ we define

$$\boldsymbol{A} \coloneqq s\boldsymbol{E} + \boldsymbol{H} = \boldsymbol{E} \coloneqq \begin{bmatrix} \alpha(R+sL) & (1-\alpha)(R+sL) & 1 & -1 \\ 1 & -1 & s\beta C & s(1-\beta)C \\ 1 & 0 & 0 & 0 \\ 0 & 1 & 0 & 0 \end{bmatrix},$$

and now proceed to obtain $\boldsymbol{Z}$ such that $\boldsymbol{A}\boldsymbol{Z} = \boldsymbol{0}$. In fact, from the last two rows we obtain $Q_d = Q_p = 0$, and then the first row gives $P \coloneqq P_d = P_p$ and finally the second one yields

$$s\beta CP + s(1-\beta)CP = sCP = 0.$$

As $s, C > 0$, we obtain $P = 0$ and thus $\boldsymbol{x} = 0$, which concludes the proof. ∎

Remark 3.2. Robin boundary conditions represent resistance conditions linearly relating pressure and blood flow rate and can be easily handled by our model. For example, if we denote by $\Omega_{\text{myocardium}}$ the domain defined by the myocardium, the interface conditions used in the 3D-0D coupling from [DGFP+20] between the lumped FSI model (0D) and the porous media (3D) at the network outlet would be obtained by setting the last equation with $\gamma_{2qd} = \alpha^{-1} > 0, \gamma_{2pd} = 1, \gamma_{2qp} = \gamma_{2pp} = 0, b_4(t) = \frac{1}{|\Omega_{\text{myocardium}}|}\int_{\Omega_{\text{myocardium}}} p\,dX$. In cardiac perfusion, these conditions are useful to alleviate the spurious pressure gradient that arises when considering pressure continuity between the vessel outlets and the average pressure in the first compartment. Indeed, the pressure in a compartment represents a predefined resolution of vessels, where

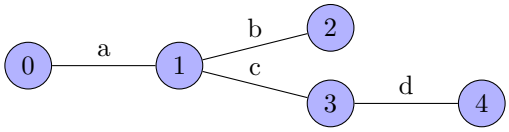

FIG. 3.1. *Example network. The segments are given by* $\mathcal{S} = \{a, b, c, d\}$ *and the nodes by* $\mathcal{N} = \{0, 1, 2, 3, 4\}$. *The inlet segments are given by* $S_0^i = \emptyset$, $S_1^n = \{a\}$, $S_2^n = \{b\}$, $S_3^i = \{c\}$, *and* $S_4^i = \{d\}$; *the outlet segments are given by* $S_0^o = \{a\}$, $S_1^o = \{b, c\}$, $S_2^o = \emptyset$, $S_3^o = \{d\}$, *and* $S_4^o = \emptyset$.

there is higher pressure at the inlets and lower pressure at the outlets. Pressure continuity should be imposed at the inlets of the compartment, so that considering the average creates a physically nonexistent pressure difference.

3.2. Network of 0D vessels. We now formalize the coupling among consecutive vessel segments, where we note that the resulting structure is that of a forest graph [CCPS09], i.e., the union of connected acyclic graphs. Consider a set of segments $\mathcal{S}$, where we identify each segment by its distal and proximal nodes as $s = \{n_d, n_p\}$. The set of all nodes will be denoted with $\mathcal{N}$, and for a given node $n \in \mathcal{N}$ we consider its inlet and outlet segments, S_n^i and S_n^o, respectively. We show an example of a bifurcation network in Figure 3.1.

Each segment can be described by (3.1) with $Q^s = \alpha^s Q_d^s + (1-\alpha^s) Q_p^s$ (P^s defined analogously), so that the following holds for all $s \in \mathcal{S}$:

$$\begin{aligned} L^s \frac{dQ^s}{dt} + R^s Q^s + P_d^s - P_p^s &= 0, \\ C^s \frac{dP^s}{dt} + Q_d^s - Q_p^s &= 0, \\ Q^s(0) &= Q_0^s, \\ P^s(0) &= P_0^s. \end{aligned} \tag{3.4}$$

The network begins at its *inflow* segments $\mathcal{S}^{\text{in}}$ and ends at its *outflow* segments $\mathcal{S}^{\text{out}}$, given by

$$\mathcal{S}^{\text{in}} := \{s \in \mathcal{S} : S_{n_p}^i = \emptyset\} \quad \text{and} \quad \mathcal{S}^{\text{out}} := \{s \in \mathcal{S} : S_{n_d}^o = \emptyset\}.$$

For each node $n \in \mathcal{N}$, the interface conditions are given by mass conservation and pressure continuity:

$$\sum_{i \in \mathcal{S}_n^i} Q_d^i = \sum_{j \in \mathcal{S}_n^o} Q_p^j \quad \forall n \in \mathcal{N}, \quad P_d^i = P_p^j \quad \forall i \in \mathcal{S}_n^i, j \in \mathcal{S}_n^o.$$

We consider in practice boundary conditions of type (NN) as we impose pressure in both inlets and outlets of the network through $P_p^s = \widehat{P}_{\text{in}}^s$ for all $s \in \mathcal{S}^{\text{in}}$ and $P_d^s = \widehat{P}_{\text{out}}^s$ for all $s \in \mathcal{S}^{\text{out}}$. More details on the form of $\widehat{P}_{\text{in}}^s, \widehat{P}_{\text{out}}^s$ will be given in section 4. For numerical tests regarding the initialization of the model, its conditioning, and its dependence on the parameters α and β, see Appendix A.

4. Coupled perfusion problem and solution strategy. In this section we present the coupling between blood flow in the epicardial coronary vessel and myocardial perfusion. The resulting model can be thought as a sequence of three events:

1. The aortic pressure p_{ao} determines the inlet blood flow in the coronary tree.
2. The blood flows through the epicardial coronaries into the tissue.
3. The blood leaves the tissue through the veins, whose pressure equals p_{veins}.

We highlight the importance of accounting for the aortic pressure p_{ao} and the venous pressure p_{veins}, as they establish the connection between our perfusion model and systemic circulation, meaning that our model yields a closed loop of blood flow in the human body.

Cardiac perfusion presents very complex spatial interactions. In this regard, a crucial process is the pressure balance between each epicardial coronary vessel and the region it perfuses. To model this, for each epicardial coronary vessel $s \in \mathcal{S}^{\text{out}}$, we associate to its outlet the region Ω_o of the myocardium, which should be perfused by it as described in [DGFP+20], referred to as the perfusion region [CLM+12, DGFP+20] and such that $\overline{\Omega} = \cup_{o \in \mathcal{S}^{\text{out}}} \overline{\Omega_o}$ (see "Coupling" in Figure 1.1). Blood flow is connected through each of the aforementioned components as follows.

Inlet pressure. We enforce the same pressure at the inlet segments (see the epicardial coronary vessels in Figure 1.1) as they both stem from the aortic root:

$$P_p^s = p_{\text{ao}} \quad \forall s \in \mathcal{S}^{\text{in}}.$$

Coupling of epicardial coronary vessels with myocardium. The outputs of the network representing the epicardial coronary vessels have an assigned pressure equal to the average pressure in the first compartment, i.e.,

$$P_d^o = \frac{1}{|\Omega_o|} \int_{\Omega_o} p_1 \, dX \quad \forall o \in \mathcal{S}^{\text{out}}. \tag{4.1a}$$

The coronaries act on the myocardium through a source term that equals the surface flow on the output. For this, we compute the source term as

$$\theta_1 \Big|_{\Omega_o} = \frac{1}{|\Omega_o|} Q^o = \frac{\alpha^o Q_d^o + (1-\alpha^o) Q_p^o}{|\Omega_o|} \quad \forall o \in \mathcal{S}^{\text{out}}. \tag{4.1b}$$

The venous return. The last compartment interacts with the veins through a sink term proportional to their pressure difference:

$$\theta_{N_C} = -\gamma (p_{N_C} - p_{\text{veins}}), \tag{4.1c}$$

where $\gamma = 10^{-4}$ [MCC+13] and $p_{\text{veins}} = 1\,\text{kPa}$ [CGSMVC10].

Remark 4.1. The feedback of the myocardium on the coronaries shown in (4.1a) can generate an artificial pressure gradient between the vessels and the myocardium. This can can be alleviated through the Robin condition shown in Remark 3.2

Remark 4.2. We recall that, in practice, we consider $N_C = 2$, which yields $p_1 = p_{\text{art}}$ and $p_2 = p_{\text{cap}}$.

For the sake of notation, we introduce suitable matrices $\boldsymbol{E}, \boldsymbol{H}$ to rewrite problem (3.4) in compact form as

$$\boldsymbol{E}\dot{\boldsymbol{Z}} + \boldsymbol{H}\boldsymbol{Z} = \boldsymbol{0}$$

using $\boldsymbol{Z} = (Q_d^1, Q_p^1, P_d^1, P_p^1, ..., Q_d^{|\mathcal{S}|}, Q_p^{|\mathcal{S}|}, P_d^{|\mathcal{S}|}, P_p^{|\mathcal{S}|})$, where $|\mathcal{S}|$ is the cardinality of $\mathcal{S}$. This allows us to write the entire coupled perfusion problem encompassing problems (3.4) and (2.5) together with coupling conditions (4.1) in weak form as follows: Find

$\boldsymbol{y}_s \in L^\infty(0,T;\boldsymbol{H}^1(\Omega))$, $\varphi_i \in L^2(0,T;H^1(\Omega)) \cap C^0([0,T];L^2(\Omega))$ for $i \in \{1,...,N_C\}$ and $\boldsymbol{Z} \in C^0([0,T];\mathbb{R}^{4|\mathcal{S}|})$ such that

(4.2a)
$$\int_\Omega (\boldsymbol{P}+\boldsymbol{P}_a(\boldsymbol{F})) : \nabla \boldsymbol{y}_s{}^*\, dX - \int_{\partial\Omega} \boldsymbol{g}(\boldsymbol{y}_s)\cdot \boldsymbol{y}_s{}^*\, dS = 0 \qquad \forall \boldsymbol{y}_s{}^* \in \boldsymbol{H}^1(\Omega),$$
$$\int_\Omega \frac{d\varphi_i}{dt}\varphi_i^* + \boldsymbol{K}_i(\boldsymbol{F})\nabla p_i \cdot \nabla \varphi_i^* + J\sum_{j=1}^{N_C}\beta_{ij}(p_i-p_j)\varphi_i^*\, dX = \int_\Omega J\theta_i\varphi_i^*\, dX \qquad \forall \varphi_i^* \in H^1(\Omega),$$
$$\boldsymbol{P} = \frac{\partial \Psi}{\partial \boldsymbol{F}}(\boldsymbol{F},\boldsymbol{\varphi}), \quad p_i = \frac{\partial \Psi}{\partial \varphi_i}(\boldsymbol{F},\boldsymbol{\varphi})$$

for all $i \in \{1,...,N_C\}$ with

$$\theta_i = \begin{cases} \frac{1}{|\Omega_o|}Q^o = \frac{\alpha^o Q_d^o + (1-\alpha^o)Q_p^o}{|\Omega_o|}, & i = 1\ \forall o \in \mathcal{S}^{\text{out}}, \\ -\gamma(p_{N_C} - p_{\text{veins}}), & i = N_C, \\ 0, & i \in \{1, N_C\}^c, \end{cases}$$

and

(4.2b)
$$\begin{aligned} &\boldsymbol{E}\dot{\boldsymbol{Z}} + \boldsymbol{H}\boldsymbol{Z} = \boldsymbol{0}, \\ &P_p^i = p_{\text{ao}} \quad \forall i \in \mathcal{S}^{\text{in}}, \\ &P_d^o = \frac{1}{|\Omega_o|}\int_{\Omega_o} p_1\, dX \quad \forall o \in \mathcal{S}^{\text{out}}. \end{aligned}$$

In view of coupling this model with the systemic circulation, we consider aortic and myocardial venous pressures as functions of deformation, which yields $p_{\text{ao}} = p_{\text{ao}}(\boldsymbol{y}_s)$ and $p_{\text{veins}} = p_{\text{veins}}(\boldsymbol{y}_s)$. Models for coupling the aortic pressure to the heart contraction are well established in the literature and are mainly based on the Windkessel model (see [WLW09] for further references). For a complete systemic circulation model coupled with the mechanics, see [RSA+20a, RSA+20b].

4.1. The one-way coupling hypothesis. We propose to neglect the influence of the blood on the tissue, by therefore assuming that $\frac{\partial \Psi}{\partial \boldsymbol{F}} \approx \frac{\partial \psi_{\text{skel}}}{\partial \boldsymbol{F}}$. This is a modeling hypothesis, which allows us to rewrite (2.5a) as

$$-\operatorname{div}(\boldsymbol{P}(\boldsymbol{F}) + \boldsymbol{P}_a(\boldsymbol{F})) = \boldsymbol{0} \quad \text{in} \quad \Omega_0, \tag{4.3}$$

where the effect of blood on the mechanics is no longer considered. The perfusion problem under this hypothesis is such that mass conservation (2.5b) is decoupled from (2.5a), so we refer to it as the one-way coupling hypothesis. In fact, this is what happens when cardiac displacement is obtained from medical images.

This approach of course neglects the important role of blood pressure during contraction, but it also has several advantages: (i) the computationally expensive electromechanics problem can be solved before the perfusion and quasi-incompressible models already take into account the volume variations of the myocardium due to blood flow, (ii) the incorporation of perfusion into an existing electromechanics software is minimally invasive as it would not require modifying the existing code, and (iii) it allows for perfusion to be appended to a cardiac imaging pipeline which obtains displacement tailored to patient-specific data. This last point is fundamental, as it puts into evidence that the use of cardiac deformation obtained from medical images implies modeling assumptions.

4.2. Numerical solver for the one-way coupled model. In this section we propose a numerical strategy for the solution of the proposed perfusion model (4.2) under the one-way coupling hypothesis. It consists in first performing an entire (electro)mechanics simulation with systemic circulation and then solving the perfusion problem, where the coupling between the porous medium and the epicardial coronary vessels is handled through a fixed point algorithm, which has been tested in the linear setting in [DGFP+20]. For this purpose, we adopt an implicit discretization method (4.2) with time step Δt. For an arbitrary quantity η, denote $\eta(t_n) \approx \eta^n$ and define the relevant, discretized in time subproblems as follows.

The epicardial coronary vasculature problem. Given $\boldsymbol{\varphi}^{n,k}$ a vector of Lagrangian porosities, find $\boldsymbol{Z}^{n,k+1}$ in $\mathbb{R}^{4|\mathcal{S}|}$ such that

$$
\begin{aligned}
(\boldsymbol{E} + \Delta t(1-\theta)\boldsymbol{H})\boldsymbol{Z}^{n,k+1} &= (\boldsymbol{E} - \Delta t\theta\boldsymbol{H})\boldsymbol{Z}^{n-1}, \\
P_p^i &= p_{\mathrm{ao}}^n \quad \forall i \in \mathcal{S}^{\mathrm{in}}, \\
P_d^o &= \frac{1}{|\Omega_o|}\int_{\Omega_o} p_1(\boldsymbol{F}^n, \boldsymbol{\varphi}^{n,k})\, dX \quad \forall o \in \mathcal{S}^{\mathrm{out}}.
\end{aligned} \tag{4.4}
$$

The myocardium problem. Given an epicardial coronary vessel solution $\boldsymbol{Z}^{n,k+1}$, find a vector of Lagrangian porosities $\boldsymbol{\varphi}^{n,k+1}$ in $\boldsymbol{H}^1(\Omega)$ such that for all $i \in \{1, ..., N_C\}$ it holds that

(4.5)

$$
\begin{aligned}
&\int_\Omega \frac{\varphi_i^{n,k+1}}{\Delta t}\varphi_i^* + \boldsymbol{K}_i(\boldsymbol{F}^n)\nabla p_i^n \cdot \nabla\varphi_i^* \\
&\qquad + J\sum_{j=1}^{N_C}\beta_{ij}(p_i^n - p_j^n)\varphi_i^*\, dX = \int_\Omega \left(J\theta_i(\boldsymbol{Z}^{n,k+1}) + \frac{\varphi_i^{n-1}}{\Delta t}\right)\varphi_i^*\, dX \qquad \forall \varphi_i^* \in H^1(\Omega), \\
&\qquad\qquad p_i^n = \frac{\partial \Psi}{\partial \varphi_i}(\boldsymbol{F}^n, \boldsymbol{\varphi}^{n,k+1}).
\end{aligned}
$$

We write this solution strategy as the pseudoalgorithm shown in Algorithm 4.1. For the mechanics, we consider the electromechanics model with systemic circulation proposed in [RSA+20a, RSA+20b, PRS+21], whose output is shown in Figure 1.1 (aortic pressure and PV loop).

5. Application to the perfusion of the heart. In what follows we present a perfusion model that integrates electromechanics, systemic circulation, and myocardial perfusion. More precisely, we consider a simulation of the entire coupled problem (4.2) on a realistic left ventricle geometry under the one-way coupling hypothesis.

5.1. The anatomical heart model and the physical parameters. The geometry used for simulations is part of the realistic anatomical template developed by the Zygote company,[2] from which we extract the left ventricle and the corresponding coronary vessels, meaning that we consider only the vessels which supply the left ventricle. The geometrical properties of the epicardial coronary vessels are extracted using VMTK [ISMA18] and used to formulate the networks. Because of the limited resolution of standard, noninvasive imaging techniques, the reconstructed geometry of the coronary tree presents a small number of vessels that initially yields unbalanced perfusion. To alleviate this, we have modified the area of each segment to obtain a more homogeneous inflow. The details about the coronary network setup are provided in Appendix B.

[2] http://www.zygote.com.

Algorithm 4.1 Perfusion problem solution algorithm.

Input: Initial displacement $\boldsymbol{y}^0$, Lagrangian porosities $\boldsymbol{\varphi}^0$ and epicardial coronary flow $\boldsymbol{Z}^0$; tolerance `tol` and maximum iterations `maxit`
Mechanics: Solve (4.3) to obtain $\boldsymbol{y}^n, p^n_{\text{ao}}, p^n_{\text{veins}}$ for each time step n
Perfusion:
for time step $n = 1, ..., T$: **do**
  Set `error` $= 1$, `k` $= 0$, $\boldsymbol{Z}^{n,0} = \boldsymbol{Z}^{n-1}$, and $\boldsymbol{\varphi}^{n,0} = \boldsymbol{\varphi}^{n-1}$
  while `error` $>$ `tol` and `k` $<$ `maxit` **do**
    Given $\boldsymbol{\varphi}^{n,k}$, compute $\boldsymbol{Z}^{n,k+1}$, which solves (4.4)
    Given $\boldsymbol{Z}^{n,k+1}$, compute $\boldsymbol{\varphi}^{n,k+1}$, which solves (4.5)
    Update `error` using $\boldsymbol{Z}^{n,k}, \boldsymbol{Z}^{n,k+1}, \boldsymbol{\varphi}^{n,k}, \boldsymbol{\varphi}^{n,k+1}$
    `k` $=$ `k` $+ 1$
  end while
  Set $\boldsymbol{Z}^n = \boldsymbol{Z}^{n,k}, \boldsymbol{\varphi}^n = \boldsymbol{\varphi}^{n,k}$
end for
return Displacement $\boldsymbol{y}^n$, Lagrangian porosities $\boldsymbol{\varphi}^n$, and epicardial flow $\boldsymbol{Z}^n$ for each time step n

TABLE 5.1
Physical parameters used in the anatomical heart model together with their corresponding reference. We highlight in bold font the parameter κ_s, as it is the only parameter that we added to the model and that we had to manually tune.

Param.	Value	Units	Ref.	Param.	Value	Units	Ref.
C_{el}	880	Pa	[ULM02]	$c_{\text{cap},3}$	10	1	[BADS88]
b_f	8	1	[ULM02]	$p_{\text{art,ref}}$	5182.15	Pa	[BADS88]
b_s	6	1	[ULM02]	$p_{\text{cap,ref}}$	2140.32	Pa	[BADS88]
b_n	3	1	[ULM02]	$\boldsymbol{K}_{f,\text{art}}$	10^{-9}	$\text{m}^2(\text{Pa s})^{-1}$	[MCC+13]
b_{fs}	12	1	[ULM02]	$\boldsymbol{K}_{f,\text{cap}}$	10^{-8}	$\text{m}^2(\text{Pa s})^{-1}$	[MCC+13]
b_{fn}	3	1	[ULM02]	$\beta\text{art, cap}$	$3.5 \cdot 10^{-5}$	$(\text{Pa s})^{-1}$	[MCC+13]
b_{sn}	3	1	[ULM02]	E	10^9	Pa	[KNSF13]
κ	$5 \cdot 10^4$	Pa	[ULM02]	ν	0.49	1	[KSKN16]
$c_{\text{art},1}$	1.33	Pa	[BADS88]	H	10^{-3}	m	[PJC+13]
$c_{\text{cap},1}$	22	Pa	[BADS88]	μ_f	0.035	Pa s	[BM03]
$c_{\text{art},2}$	550	Pa	[BADS88]	ρ_f	1060	kg/m^3	[BM03]
$c_{\text{cap},2}$	1009	Pa	[BADS88]				
$c_{\text{art},3}$	45	1	[BADS88]	$\boldsymbol{\kappa_s}$	$\mathbf{5 \cdot 10^4}$	**Pa**	**-**

We present the anatomically relevant parameters used in our model in Table 5.1. Note that the value $\kappa_s = 5 \cdot 10^4$ is the only parameter that we added, and so we had to adjust it manually. It is set to almost equally balance the quasi-incompressibility constraint enforced on J and φ_s. As detailed in [CM14], it is fundamental that both effects coexist, but a detailed characterization of their interaction remains understudied.

5.2. Results. The main output of the myocardial perfusion model is shown in Figures 5.1 and 5.2. The main quantities of interest are the pressure, the added mass, and the coronary flow. In Figure 5.1 we show the average value of these variables calculated on the ventricle, whereas in Figure 5.2 we illustrate time snapshots of the entire added mass field in the ventricle. The convergence of the fixed point method is smooth, as it takes no more than 10 iterations to satisfy the tolerance of 10^{-3} with respect to the maximum relative increment between both physics in all of the numerical tests we performed.

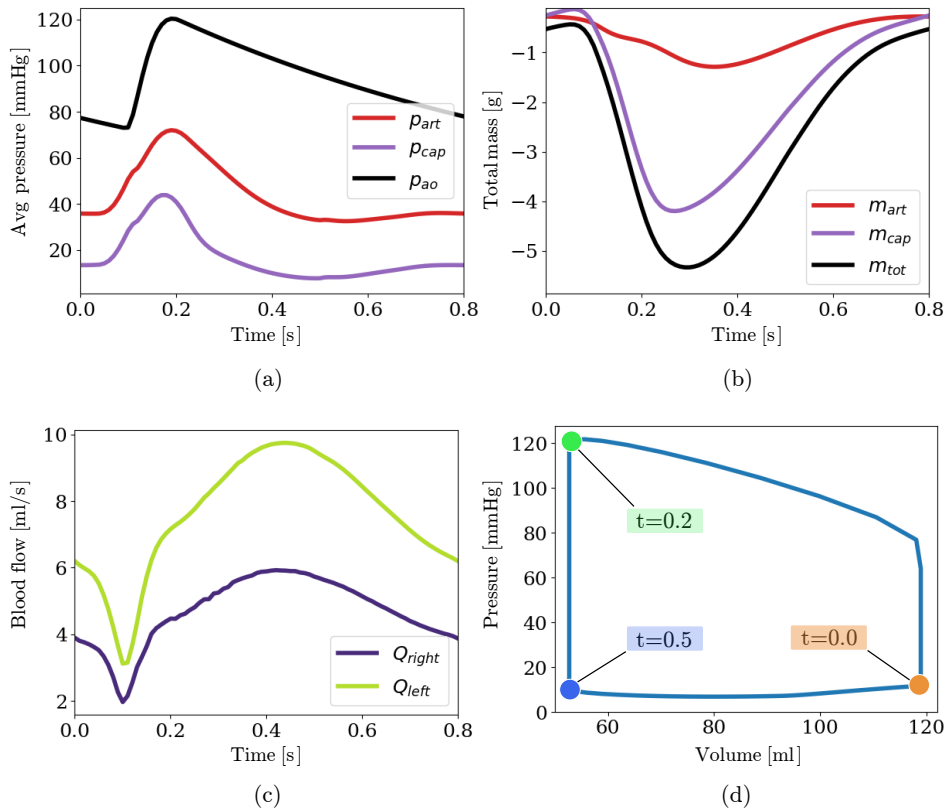

FIG. 5.1. *Evolution of global quantities of the myocardial perfusion model: average pressure, total added mass, and blood flow, with the PV loop for reference.*

Figure 5.1 aims at illustrating the input-output interactions captured by the proposed model. Panel (a) reports a significant pressure drop along the coronary tree, from the main vessels to the capillaries. The pressure waveform remains anyway almost unperturbed. Without the myocardial contraction, this waveform would propagate also to the added mass and the coronary flow, but as we see from panels (b) and (c), this is not the case. Instead, these results suggest that the heart contraction regulates the perfusion process and in fact the added mass plot in time drops at the systole. In correspondence to the steepest decrease of the added mass, we observe that the flow in the coronaries reaches a minimum, while it increases significantly during the diastole. This effect is called the *systolic impediment* and it is a distinctive trait of blood flow in the myocardium. The ability of the model to capture this effect on the basis of the interaction between aortic pressure and mechanical contraction, without any specific bias that could trigger it, is one of the most relevant outcomes of the presented model. We further stress that this model was solved by means of our one-way coupling hypothesis, suggesting that the feedback of the blood on the tissue is not essential to reproduce the systolic impediment.

To the best of our knowledge, only [NLL+20] and [CLM+12] propose a myocardial perfusion model coupled with systemic circulation exhibiting the systolic impediment. We note that the model of [CLM+12] considers a flow as input to the coronary vessels;

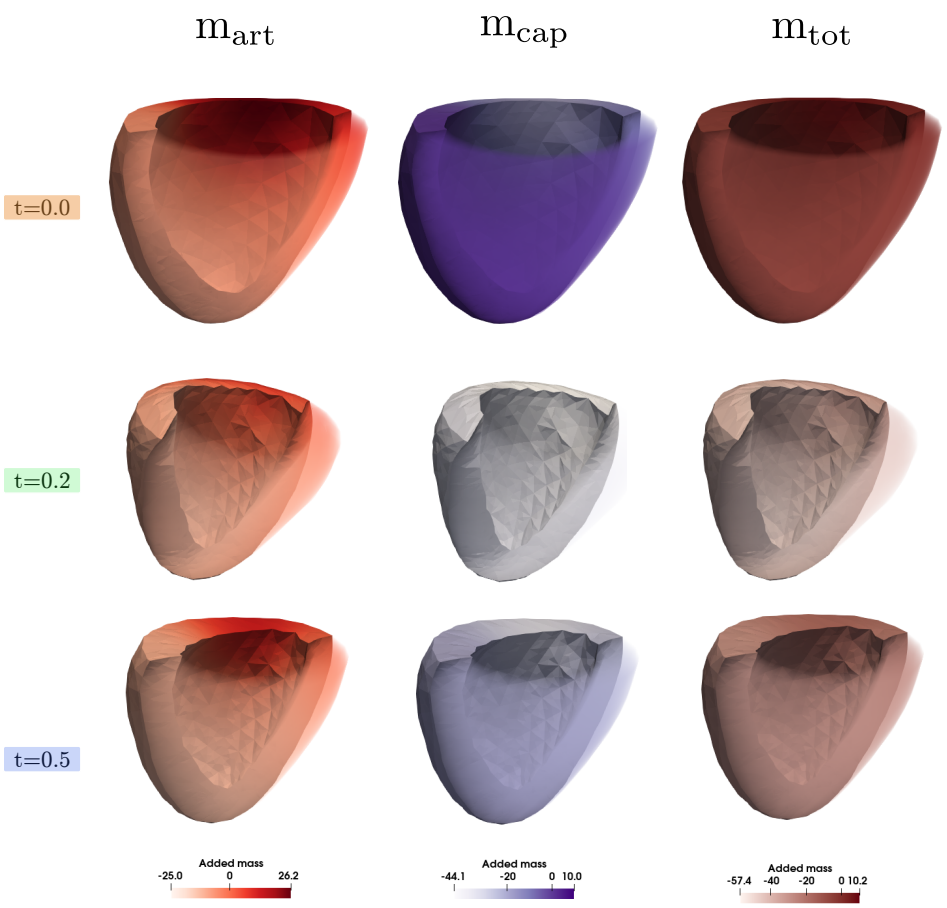

FIG. 5.2. *Evolution of the local added masses in arteries and capillaries, together with their global contribution. Chosen instants are shown in the PV loop in Figure* 5.1.

in this way systolic impediment is given externally by the boundary conditions. This is not the case for the one presented in [NLL+20], which has two main differences with respect to ours: (i) incompressibility ($J = 1$) and an ad hoc relationship for the intramyocardial pressure depending only on mechanic variables are assumed and (ii) the porous media is replaced by a complex network of vessels reconstructed from morphometric swine measurements representing the entire coronary vasculature (epicardial and myocardial). Our work addresses the problem from the fundamental thermodynamic principles of the physics involved and in consequence yields comparable results under fewer hypotheses in a computationally flexible framework.

6. Conclusions. In this work we presented a mathematical model for cardiac perfusion and its coupling with systemic circulation. More precisely, we developed a multicompartment poromechanics model for the perfusion of the myocardium and a lumped FSI model for the blood flow in the epicardial coronary vessels. The coupling with the systemic circulation was performed through the aortic and myocardial venous

pressures. Using a one-way coupling strategy to solve numerically this coupled problem, we were able to reproduce the systolic impediment, which is a distinctive feature of myocardial perfusion. This result was possible due to the interaction between the pressure in the coronary microvasculature and the aortic pressure, and it shows that the main driver of perfusion is the contraction of the heart. The novel poroelastic potential described in this work considers the fluid porosity in all compartments and quasi-incompressibility for both the geometry and the solid phase. In contrast to other approaches, it has the advantage to ease the computational cost of the problem as it does not require the use of additional multiplier variables. Moreover, it entails the fundamental result that the pressure acting on the myocardial coronary vessels is given by the difference between the intramyocardial and intravascular pressures. We highlight that this is not an ad hoc choice but a consequence of the considered potential, meaning that our model is thermodynamically consistent. We also devised unified conditions under which the proposed potential guarantees the existence of solutions to both the mechanics and the porous media problems (independently). Besides the analytic relevance of this result, it states that convexity is essential for all of the porous media potentials.

Appendix A. Numerical tests on the vessel network. In this appendix we numerically study the lumped network model. In particular, we focus on the conditioning of the resulting linear system, its initialization by means of finding a steady state relative to the initial boundary conditions $(\widehat{P}^s_{\text{in}}, \widehat{P}^s_{\text{out}})$, and its dependence on the parameters α and β. For all tests we consider the bifurcation network from Figure 3.1 with the parameters described in section 5.1.

A.1. Problem conditioning. The different scales of the problem parameters can give rise to poor conditioning. In vascular modeling, the area of a coronary is small ($A \approx 10^{-6}\text{m}^2$), which yields large resistance terms $R = O(A^{-2}) \approx 10^{12}$. After discretizing in time, we compute the conditioining number of the resulting matrix with NumPy [Oli06]. To alleviate the bad scaling of the resistance terms, we consider a diagonal preconditioner P which values 1 and R in the rows corresponding to pressure and flow degrees of freedom, respectively.

We compute the condition number in the following scenarios: (i) with vs. without diagonal preconditioner $\boldsymbol{P}$, (ii) SI units (m, kg, s, Pa) vs. scaled units (cm, g, s, kPa), and (iii) $\alpha^s = \beta^s = \chi \in \{0, 0.5, 1\}$ for all $s \in \mathcal{S}$. We used the same parameters as the ones used for the complete heart simulation, where the inlet pressure is p_{ao} and the oulet pressure is 9 kPa in all outlets. The results obtained are shown in Table A.1, where we note that the proposed preconditioner works well in all scenarios. The problem in general presents much better conditioning with the scaled units (cm, g, s, kPa), and interestingly, mixing the variables through $\alpha = 0.5$ improves the matrix conditioning.

TABLE A.1
Condition number for the reduced network models.

Scenario	$\chi = 0$	$\chi = 0.5$	$\chi = 1$
No prec, SI	$2.01 \cdot 10^{18}$	$1.29 \cdot 10^{18}$	$1.33 \cdot 10^{18}$
Prec, SI	$3.58 \cdot 10^{12}$	$3.34 \cdot 10^{11}$	$3.91 \cdot 10^{11}$
No prec, scaled	$3.64 \cdot 10^{7}$	$7.15 \cdot 10^{5}$	$4.45 \cdot 10^{7}$
Prec, scaled	$8.27 \cdot 10^{6}$	$1.63 \cdot 10^{5}$	$1.01 \cdot 10^{7}$

TABLE A.2
Iterations required to achieve a stationary state with and without acceleration for different values of χ and acceleration depths.

# iterations	$\chi = 0$	$\chi = 0.5$	$\chi = 1$
No accel.	4617	4617	4617
Anderson(1)	2172	2336	1075
Anderson(2)	98	75	102

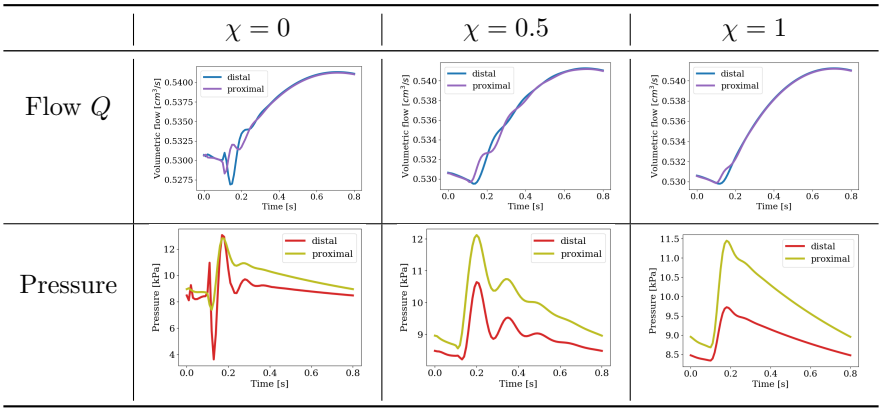

FIG. A.1. *Flow and pressure for mixing sensitivity test in segment "c."*

A.2. Steady initial conditions. The time-dependence of model (3.4) is what gives it the ability to incorporate inertia and compliance, but it means that it is sensitive to initial conditions. To obtain realistic initial conditions, we propose performing simulation with the boundary conditions fixed at $t = t_0$ until a steady state is achieved. The time required to achieve a steady solution can be large, so we additionally use Anderson acceleration [WN11] until a stationary solution is obtained.

A relative tolerance of 10^{-10} on the residual yields the iteration counts shown in Table A.2, where the effect of acceleration can be neatly appreciated, yielding an overall iteration count reduction of 75% to 50% for one level of acceleration and roughly 98% for two levels. Three or more levels do not converge, and the two-levels scenario required using a delay of five iterations.

A.3. Dependence on α and β. In this section we study the impact that the choice of α and β has on the solution. We consider the inlet pressure profile p_{ao} shown in Figure 1.1 and an outlet of $9\,kPa$, with all solutions given by the steady dynamic. We show in Figure A.1 the results of flow and pressure simulated in segment c of the bifurcation network depicted in Figure 3.1. The case $\alpha = 0$ yields pressure drops below the outlet pressure with also unrealistic oscillations. Case $\alpha = \beta = \chi = 1$ presents a physiological response and is much stiffer, as seen, for example, in the minimal difference between distal and proximal flows in all segments. Finally, case $\chi = 0.5$ presents a solution similar to $\chi = 1$, but presents more oscillations. This shows that the latter has the potential to capture more precisely vessel compliance.

Appendix B. Additional details about the model setup. The perfusion regions are visualized in Figure 1.1 in the panel *Heart geometry* with different colors

on the epicardial surface. The heterogeneity of their physical properties makes it difficult to solve the equation

$$\frac{d\varphi_i}{dt} - \operatorname{div}\left(\boldsymbol{K}_i(\boldsymbol{F})\nabla p_i\right) + J\sum_{j=1}^{N_C}\beta_{ij}(p_i - p_j) = J\theta_i$$

for two main reasons. The first is the abrupt variation of the source terms $J\theta_i$ from region to region, which depends on the distribution of the flow at the endpoints of the coronary tree. The second one is the ratio between the permeabilities $|\boldsymbol{K}_i(\boldsymbol{F})|$ and the parameters β_{ij} that regulate the interactions between compartments. Abrupt spatial variations of θ_i may worsen the conditioning of the problem, as observed in the numerical experiments. For this reason, starting from the rough anatomical data, a few calibration steps were necessary to mitigate these difficulties. More precisely, two additional calibration steps were adopted, one for the network model and one for the porous media; we give the corresponding details in what follows.

Network model. The epicardial coronary vessels computed from the Zygote geometry yielded highly concentrated blood inflows in certain perfusion regions, leaving the other regions without a proper blood supply. This results in a high spatial heterogeneity of the terms $J\theta_i$, which causes issues in the convergence of the linear solvers. We recall that the terms $J\theta_i$ depend on the outflow of the coronary tree. For this reason, to improve the distribution of these flows, we act on the vessel cross sections at the interface between the 0D and the 3D models. In order to compute a more homogeneous blood inflow, we used two procedures, a global and a local vessel correction:

- *Global correction.* We included an amplifying factor ξ in the vessel areas A_s for all segments s (see section 3), so that the new areas are given by $\tilde{A}_s = \xi A_s$ for all segments s. We have found $\xi = 2$ to give realistic results.
- *Local correction.* We used perfusion simulations without deformation, then halved the area of all terminal vessels yielding hyper-perfused regions and also doubled the area of all terminal vessels yielding hipo-perfused regions. This was iterated until the blood distribution was roughly homogeneous. Whenever doubling/halving proved too coarse, we used the smaller factors x0.75 and x1.5, and also whenever terminal vessels would not provide satisfactory results, we modified the areas of additional (nonterminal) vessels. The original and modified vessel areas are shown in Table B.1, where the numbers follow the vessel numbering shown in Figure B.1.

Porous media. After adjusting vessel areas for obtaining a better balanced source term, our linear solver still diverged after a few time steps. This happened

TABLE B.1
Modified vessel areas for Zygote coronaries in $10^{-6}\,m^2$.

	2	3	4	6	7	8	9	10	16	17	19	20
Original	0.77	0.52	1.23	0.86	1.43	1.79	2.25	1.49	0.92	0.94	0.52	0.5
Modified	0.77	1.32	1.23	0.86	0.22	1.79	4.51	2.96	1.844	2.99	0.52	0.75
	21	22	23	24	25	26	28	29	30	32	33	34
Original	0.50	1.02	6.49	3.79	3.74	3.58	4.09	2.34	1.95	2.59	1.74	1.57
Modified	0.50	1.02	6.49	3.79	3.74	3.58	4.09	2.34	1.95	1.3	1.045	1.50

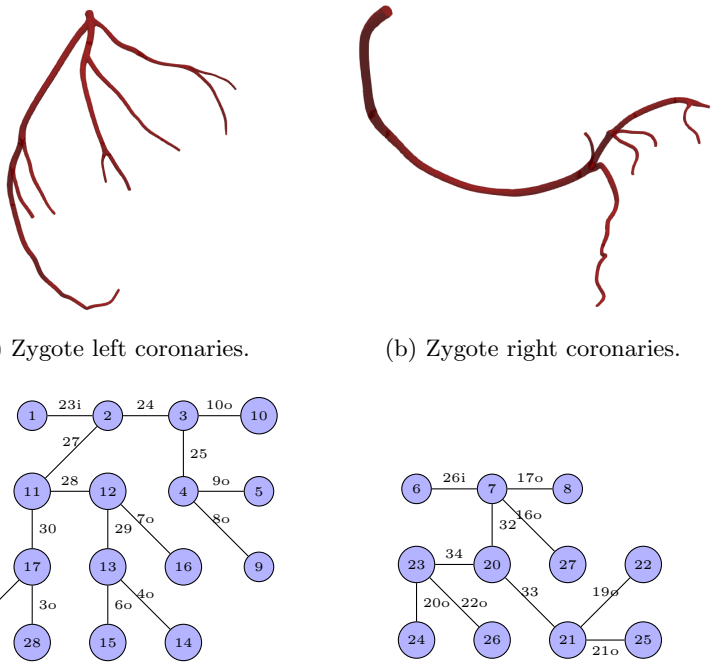

(a) Zygote left coronaries.

(b) Zygote right coronaries.

(c) Reduced model and tags of left coronaries.

(d) Reduced model and tags of right coronaries.

FIG. B.1. *Left coronary tree model reduction. Inlet and outlet segments denoted with "i" and "o," respectively.*

only when testing a multicompartment model and is explained by the presence of the pressure differences required for the interaction between compartments, namely, the term $\sum_{j=1}^{N_C} \beta_{ij}(p_i - p_j)$ in the equation above. These are reaction terms, and thus numerical instabilities are expected whenever the diffusion is sufficiently small [QV08]. In consequence, to reduce the dominance of the reaction terms and obtain a more robust numerical solver, we enlarged the permeability tensors to 10^{-7}. This problem can be better addressed by developing (i) preconditioners that are robust with respect to the permeability and (ii) adequate stabilization techniques that reduce the conditioning of reaction-dominant problems.

REFERENCES

[AANQ11] D. AMBROSI, G. ARIOLI, F. NOBILE, AND A. QUARTERONI, *Electromechanical coupling in cardiac dynamics: The active strain approach*, SIAM J. Appl. Math., 71 (2011), pp. 605–621.

[AKL10a] D. ALGRANATI, G. S. KASSAB, AND Y. LANIR, *Mechanisms of myocardium-coronary vessel interaction*, Amer. J. Physiology, 298 (2010), pp. H861–H873.

[AKL10b] D. ALGRANATI, G. S. KASSAB, AND Y. LANIR, *Mechanisms of myocardium-coronary vessel interaction*, Amer. J. Physiology, 298 (2010), pp. H861–H873.

[BADS88] P. BRUINSMA, T. ARTS, J. DANKELMAN, AND J. A. E. SPAAN, *Model of the coronary circulation based on pressure dependence of coronary resistance and compliance*, Basic Res. Cardiology, 83 (1988), pp. 510–524.

[BB00] D. A. BEARD AND J. B. BASSINGTHWAIGHTE, *The fractal nature of myocardial blood flow emerges from a whole-organ model of arterial network*, J. Vascular Res., 37 (2000), pp. 282–296.

[BBPT12] J. D. Bayer, R. C. Blake, G. Plank, and N. A. Trayanova, *A novel rule-based algorithm for assigning myocardial fiber orientation to computational heart models*, Ann. Biomed. Eng., 40 (2012), pp. 2243–2254.

[BCM17] B. Burtschell, D. Chapelle, and P. Moireau, *Effective and energy-preserving time discretization for a general nonlinear poromechanical formulation*, Comput. Struct., 182 (2017), pp. 313–324.

[BF10] P. J. Blanco and R. A. Feijóo, *A 3D-1D-0D computational model for the entire cardiovascular system*, Comput. Method. Hemodyn., 59 (2010), pp. 5887–5911.

[BM03] O. K. Baskurt and H. J. Meiselman, *Blood Rheology and Hemodynamics*, Semin. Thromb. Hemost., 29 (2003), pp. 435–450.

[Bow80] R. M. Bowen, *Incompressible porous media models by use of the theory of mixtures*, Internat. J. Engrg. Sci., 18 (1980), pp. 1129–1148.

[Bow82] R. M. Bowen, *Compressible porous media models by use of the theory of mixtures*, Internat. J. Engrg. Sci., 20 (1982), pp. 697–735.

[Cam80] S. Campbell, *Singular Systems of Differential Equations*, Vol. 1, Pitman, London, 1980.

[CCHK17] F. S. Costabal, F. A. Concha, D. E. Hurtado, and E. Kuhl, *The importance of mechano-electrical feedback and inertia in cardiac electromechanics*, Comput. Methods Appl. Mech. Engrg., 320 (2017), pp. 352–368.

[CCPS09] W. J. Cook, W. H. Cunningham, W. R. Pulleyblank, and A. Schrijver, *Combinatorial optimization*, Oberwolfach Rep., 5 (2009), pp. 2875–2942.

[CGSMVC10] D. Chapelle, J. F. Gerbeau, J. Sainte-Marie, and I. E. Vignon-Clementel, *A poroelastic model valid in large strains with applications to perfusion in cardiac modeling*, Comput. Mech., 46 (2010), pp. 91–101.

[CLM+12] A. N. Cookson, J. J. Lee, C. Michler, R. Chabiniok, E. Hyde, D. A. Nordsletten, M. Sinclair, M. Siebes, and N. P. Smith, *A novel porous mechanical framework for modelling the interaction between coronary perfusion and myocardial mechanics*, J. Biomech., 45 (2012), pp. 850–855.

[CM14] D. Chapelle and P. Moireau, *General coupling of porous flows and hyperelastic formulations—From thermodynamics principles to energy balance and compatible time schemes*, Eur. J. Mech. B Fluids, 46 (2014), pp. 82–96.

[Cou04] O. Coussy, *Poromechanics*, John Wiley & Sons, New York, 2004.

[CWH+16] R. Chabiniok, V. Y. Wang, M. Hadjicharalambous, L. Asner, J. Lee, M. Sermesant, E. Kuhl, A. A. Young, P. Moireau, M. P. Nash, D. Chapelle, and D. A. Nordsletten, *Multiphysics and multiscale modelling, data–model fusion and integration of organ physiology in the clinic: Ventricular cardiac mechanics*, Interface Focus, 6 (2016).

[dBCD98] P. de Buhan, X. Chateau, and L. Dormieux, *The constitutive equations of finite strain poroelasticity in the light of a micro-macro approach*, Eur. J. Mech. A Solids, 17 (1998), pp. 909–921.

[DGFP+20] S. Di Gregorio, M. Fedele, G. Pontone, A. F. Corno, P. Zunino, C. Vergara, and A. Quarteroni, *A computational model applied to myocardial perfusion in the human heart: From large coronaries to microvasculature*, J. Comput. Phys., 424 (2021), 109836.

[DGQ20] L. Dede, A. Gerbi, and A. Quarteroni, *Segregated algorithms for the numerical simulation of cardiac electromechanics in the left human ventricle*, in The Mathematics of Mechanobiology, Springer, New York, 2020, pp. 81–116.

[DJBBD92] J. T. Dodge, Jr., B. G. Brown, E. L. Bolson, and H. T. Dodge, *Lumen diameter of normal human coronary arteries. Influence of age, sex, anatomic variation, and left ventricular hypertrophy or dilation*, Circulation, 86 (1992), pp. 232–246.

[DK75] J. M. Downey and E. S. Kirk, *Inhibition of coronary blood flow by a vascular waterfall mechanism*, Circulation Res., 36 (1975), pp. 753–760.

[FAC16] D. A. Fonseca, P. E. Antunes, and M. D. Cotrim, *The morphology, physiology and pathophysiology of coronary microcirculation*, in Microcirculation Revisited—From Molecules to Clinical Practice, InTech Open, London, 2016, pp. 15–47.

[FPS14] P. C. Franzone, L. F. Pavarino, and S. Scacchi, *Mathematical Cardiac Electrophysiology*, MS&A. Model. Simul. Appl. 13, Springer, New York, 2014.

[FQV09] L. Formaggia, A. Quarteroni, and A. Veneziani, *Multiscale models of the vascular system*, in Cardiovascular Mathematics, Springer, New York, 2009, pp. 395–446.

[GDQ19] A. Gerbi, L. Dedé, and A. Quarteroni, *A monolithic algorithm for the simulation of cardiac electromechanics in the human left ventricle*, Math. in Engrg., 1 (2019), pp. 1–37.

[GMW91] J. M. Guccione, A. D. McCulloch, and L. K. Waldman, *Passive material properties of intact ventricular myocardium determined from a cylindrical model*, J. Biomech. Eng., 113 (1991), pp. 42–55.

[GPCP90] C. Guiot, P. G. Pianta, C. Cancelli, and T. J. Pedley, *Prediction of coronary blood flow with a numerical model based on collapsible tube dynamics*, Amer. J. Physiology, 258 (1990), pp. H1606–H1614.

[HAvCR92] J. M. Huyghe, T. Arts, D. H. van Campen, and R. S. Reneman, *Porous medium finite element model of the beating left ventricle*, Amer. J. Physiology, 262 (1992), pp. H1256–H1267.

[HB11] M. C. Hsu and Y. Bazilevs, *Blood vessel tissue prestress modeling for vascular fluid–structure interaction simulation*, Finite Elem. Anal. Des., 47 (2011), pp. 593–599.

[HBJ+17] M. Hirschvogel, M. Bassilious, L. Jagschies, S. M. Wildhirt, and M. W. Gee, *A monolithic 3D-0D coupled closed-loop model of the heart and the vascular system: Experiment-based parameter estimation for patient-specific cardiac mechanics*, Int. J. Numer. Methods Biomed. Eng., 33 (2017), e2842.

[HBRS08] M. R. Hoenig, C. Bianchi, A. Rosenzweig, and F. W. Sellke, *The cardiac microvasculature in hypertension, cardiac hypertrophy and diastolic heart failure*, Current Vascular Pharm., 6 (2008), pp. 292–300.

[HKL+09] Y. Huo, B. Kaimovitz, Y. Lanir, T. Wischgoll, J. I. E. Hoffman, and G. S. Kassab, *Biophysical model of the spatial heterogeneity of myocardial flow*, Biophys. J., 96 (2009), pp. 4035–4043.

[HS90] J. I. Hoffman and J. A. Spaan, *Pressure-flow relations in coronary circulation*, Physiolog. Rev., 70 (1990), pp. 331–390.

[ISMA18] R. Izzo, D. Steinman, S. Manini, and L. Antiga, *The vascular modeling toolkit: A Python library for the analysis of tubular structures in medical images*, J. Open Source Softw., 3 (2018), 745.

[KCB85] J. Y. Kresh, M. A. Cobanoglu, and S. K. Brockman, *The intramyocardial pressure: A parameter of heart contractility*, J. Heart Transplant., 4 (1985), pp. 241–246.

[KNSF13] A. Karimi, M. Navidbakhsh, A. Shojaei, and S. Faghihi, *Measurement of the uniaxial mechanical properties of healthy and atherosclerotic human coronary arteries*, Mater. Sci. Eng. C, 33 (2013), pp. 2550–2554.

[KSKN16] A. Karimi, T. Sera, S. Kudo, and M. Navidbakhsh, *Experimental verification of the healthy and atherosclerotic coronary arteries incompressibility via digital image correlation*, Artery Res., 16 (2016), pp. 1–7.

[KVCC+10] H. J. Kim, I. E. Vignon-Clementel, J. S. Coogan, C. A. Figueroa, K. E. Jansen, and C. A. Taylor, *Patient-specific modeling of blood flow and pressure in human coronary arteries*, Ann. Biomed. Eng., 38 (2010), pp. 3195–3209.

[LMR+10] G. Liew, P. Mitchell, E. Rochtchina, T. Y. Wong, W. Hsu, M. L. Lee, A. Wainwright, and J. J. Wang, *Fractal analysis of retinal microvasculature and coronary heart disease mortality*, Eur. Heart J., 32 (2010), pp. 422–429.

[LNN+09] J. Lee, S. Niederer, D. Nordsletten, I. Le Grice, B. Smail, D. Kay, and N.P. Smith, *Coupling contraction, excitation, ventricular and coronary blood flow across scale and physics in the heart*, Philos. Trans. A, 367 (2009), pp. 2311–2331.

[LS12] J. Lee and N. P. Smith, *The multi-scale modelling of coronary blood flow*, Ann. Biomed. Eng., 40 (2012), pp. 2399–2413.

[MCC+13] C. Michler, A. N. Cookson, R. Chabiniok, E. Hyde, J. Lee, M. Sinclair, T. Sochi, A. Goyal, G. Vigueras, and D. A. Nordsletten, *A computationally efficient framework for the simulation of cardiac perfusion using a multi-compartment Darcy porous-media flow model*, Int. J. Numer. Methods Biomed. Eng., 29 (2013), pp. 217–232.

[MQY94] S. Müller, T. Qi, and B. S. Yan, *On a new class of elastic deformations not allowing for cavitation*, Ann. Inst. H. Poincaré Anal. Non Linéaire 11, Elsevier, New York, 1994, pp. 217–243.

[NKL18] R. Namani, G. S. Kassab, and Y. Lanir, *Morphometric reconstruction of coronary vasculature incorporating uniformity of flow dispersion*, Front. Physiology, 9 (2018), 1069.

[NLL+20] R. Namani, L. C. Lee, Y. Lanir, B. Kaimovitz, S. M. Shavik, and G. S. Kassab, *Effects of myocardial function and systemic circulation on regional coronary perfusion*, J. Appl. Physiology, 128 (2020), pp. 1106–1122.

[Oli06] T. E. Oliphant, *A Guide to NumPy*, vol. 1, Trelgol Publishing, 2006.

[PHW+19] M. R. Pfaller, J. M. Hörmann, M. Weigl, A. Nagler, R. Chabiniok, C. Bertoglio, and W. A. Wall, *The importance of the pericardium for cardiac biomechanics: From physiology to computational modeling*, Biomech. Model. Mechanobiol., 18 (2019), pp. 503–529.

[PJC+13] R. Perry, M. X. Joseph, D. P. Chew, P. E. Aylward, and C. G. De Pasquale, *Coronary artery wall thickness of the left anterior descending artery using high resolution transthoracic echocardiography—Normal range of values*, Echocardiography, 30 (2013), pp. 759–764.

[PKJ+20] L. Papamanolis, H. J. Kim, C. Jaquet, M. Sinclair, M. Schaap, I. Danad, P. van Diemen, P. Knaapen, L. Najman, H. Talbot, C. A. Taylor, and I. Vignon-Clementel, *Myocardial perfusion simulation for coronary artery disease: A coupled patient-specific multiscale model*, Ann. Biomed. Eng., 49 (2021), pp. 1432–1447.

[PRS+21] R. Piersanti, F. Regazzoni, M. Salvador, A. F. Corno, L. Dede, C. Vergara, and A. Quarteroni, *3D-0D Closed-Loop Model for the Simulation of Cardiac Biventricular Electromechanics*, preprint, arXiv:2108.01907, 2021.

[QDMV19] A. Quarteroni, L. Dede', A. Manzoni, and C. Vergara, *Mathematical Modelling of the Human Cardiovascular System: Data, Numerical Approximation, Clinical Applications*, Cambridge Monogr. Appl. Comput. Math. 33, Cambridge University Press, Cambridge, 2019.

[QLRRB17] A. M. Quarteroni, T. Lassila, S. Rossi, and R. Ruiz-Baier, *Integrated heart–coupling multiscale and multiphysics models for the simulation of the cardiac function*, Comput. Methods Appl. Mech. Engrg., 314 (2017), pp. 345–407.

[QRV01] A. Quarteroni, S. Ragni, and A. Veneziani, *Coupling between lumped and distributed models for blood flow problems*, Comput. Vis. Sci., 4 (2001), pp. 111–124.

[QV08] A. Quarteroni and A. Valli, *Numerical Approximation of Partial Differential Equations*, Springer Ser. Comput. Math. 23, Springer, New York, 2008.

[QVV16] A. Quarteroni, A. Veneziani, and C. Vergara, *Geometric multiscale modeling of the cardiovascular system, between theory and practice*, Comput. Methods Appl. Mech. Engrg., 302 (2016), pp. 193–252.

[RSA+20a] F. Regazzoni, M. Salvador, P. C. Africa, M. Fedele, L. Dede, and A. Quarteroni, *A Cardiac Electromechanics Model Coupled with a Lumped Parameters Model for Closed-Loop Blood Circulation. Part* I*: Model Derivation*, arXiv:2011:15040, 2020.

[RSA+20b] F. Regazzoni, M. Salvador, P. C. Africa, M. Fedele, L. Dede, and A. Quarteroni, *A Cardiac Electromechanics Model Coupled with a Lumped Parameters Model for Closed-Loop Blood Circulation. Part* II*: Numerical Approximation*, arXiv:2011:15051, 2020.

[SBL81] J. A. Spaan, N. P. Breuls, and J. D. Laird, *Diastolic-systolic coronary flow differences are caused by intramyocardial pump action in the anesthetized dog*, Circulation Res., 49 (1981), pp. 584–593.

[Smi04] N. P. Smith, *A computational study of the interaction between coronary blood flow and myocardial mechanics*, Physiological Measur., 25 (2004), 863.

[ULM02] T. P. Usyk, I. J. LeGrice, and A. D. McCulloch, *Computational model of three-dimensional cardiac electromechanics*, Comput. Vis. Sci., 4 (2002), pp. 249–257.

[Váz07] J. L. Vázquez, *The Porous Medium Equation: Mathematical Theory*, Oxford University Press, Oxford, 2007.

[VSW97] M. A Vis, P. Sipkema, and N. Westerhof, *Modeling pressure-flow relations in cardiac muscle in diastole and systole*, Amer. J. Physiology, 272 (1997), pp. H1516–H1526.

[VYW15] A. T. Vuong, L. Yoshihara, and W. A. Wall, *A general approach for modeling interacting flow through porous media under finite deformations*, Comput. Methods Appl. Mech. Engrg., 283 (2015), pp. 1240–1259.

[WBDVN69] N. Westerhof, F. Bosman, C. J. De Vries, and A. Noordergraaf, *Analog studies of the human systemic arterial tree*, J. Biomech., 2 (1969), pp. 121–143.

[Whi86] S. Whitaker, *Flow in porous media* I: *A theoretical derivation of Darcy's law*, Transp. Porous Media, 1 (1986), pp. 3–25.

[WLW09] N. Westerhof, J. W. Lankhaar, and B. E. Westerhof, *The arterial Windkessel*, Med. Biol. Eng. Comput., 47 (2009), pp. 131–141.

[WN11] H. F. Walker and P. Ni, *Anderson acceleration for fixed-point iterations*, SIAM J. Numer. Anal., 49 (2011), pp. 1715–1735.